Flight data analysis of the BERM radiation monitor aboard the BepiColombo mission

António de Lagos Roque Pessanha Gomes

Thesis to obtain the Master of Science Degree in

Engineering Physics

Supervisors: Prof. Patrícia Carla Serrano Gonçalves
Dr. Marco Gui Alves Pinto

Examination Committee

Chairperson: Prof. Name of the Chairperson
Supervisor: Prof. Patrícia Carla Serrano Gonçalves
Members of the Committee: Prof. Name of First Committee Member
Dr. Name of Second Committee Member
Eng. Name of Third Committee Member

October 2023

Abstract

BepiColombo is a joint mission between the European Space Agency (ESA), and the Japan Aerospace Exploration Agency (JAXA) to explore Mercury. It consists of two spacecraft, Mercury Planetary Orbiter (MPO) from ESA and Mercury Magnetospheric Orbiter (MMO) from JAXA. The mission was launched in 2018 and it is predicted to enter Mercury's orbit in December 2025.

BepiColombo Environment Radiation Monitor (BERM) is the radiation monitor, aboard the BepiColombo, and has the task of monitoring the radiation environment. BERM was developed by ESA in cooperation with the Portuguese company EFACEC S.A. . It is designed to detect high fluxes of electrons with energies from $\sim$100 keV to $\sim$10 MeV, protons with energies from 1 MeV to $\sim$200 MeV, and heavy ions with Linear Energy Transfer from 1 to 50 MeV/mg/cm^2. It is composed of one stack of 11 silicon detectors interleaved by tantalum and aluminium. From the energy deposited in the silicon layers and the energy deposition pattern, BERM distinguishes particles in 18 channels: 5 for electrons, 8 for protons and 5 for heavy ions. The monitor provides the number of counts in each channel integrated over 30 seconds sampling intervals.

In this work, the threshold and cross-talk between BERM sensors was studied to improve the characterisation of its channels. For this purpose, several tests to the spare model of BERM using 137-Cs and 90-Sr radioactive sources were performed, and the proton calibration data from 2014 was reanalysed. A new model of the cross-talk was created and implemented in the response functions of BERM. The response functions were combined with different models of the radiation environment considered for the BERM Earth flyby and compared to the Solar Intensity X-ray Spectrometer (SIXS) instrument also aboard the BepiColombo mission for validation. The method was successful in reproducing the low energy electron data. Bow-tie reconstruction of Solar Particle Events flux was also successfully validated

with SIXS data.

Keywords

BepiColombo; BERM; Electrons; Protons; Solar Events; Mercury.

Resumo

Bepicolombo é uma missão conjunta entre a European Space Agency (ESA), e a Japan Aerospace Exploration Agency (JAXA) para explorar Mercúrio. É composta por duas naves, a Mercury Planetary Orbiter (MPO) da ESA e a Mercury Magnetospheric Orbiter (MMO) da JAXA. A missão foi lançada em 2018 e está previsto entrar em orbita de Mercúrio em Dezembro de 2025.

O BepiColombo Environment Radiation Monitor (BERM) é o monitor de radiação abordo da Bepicolombo, e tem como objetivo monitorizar a radiação ambiente. O BERM foi desenvolvido pela ESA em cooperação com a empresa Portuguesa EFACEC. Tem a capacidade de detetar elevados fluxos de eletrões com energias desde 100 KeV até 10 MeV, protões desde 1 MeV até 200 MeV e iões pesados desde 1 até 50 MeV/mg/cm^2. É composto por um conjunto de 11 detetores de silício, intercalados por tântalo e alumínio. A partir da energia depositada no silício e do padrão de deposição de energia, o BERM separa as partículas em 18 canais: 5 de eletrões, 8 de protões e 5 de iões pesados. O monitor providencia as contagens em cada canal, integradas em intervalos de 30 segundos.

Neste trabalho os thresholds do BERM e o cross-talk entre detetores foram analisados com o objetivo de melhorar a caracterização dos canais. Para tal, foram realizados vários testes com uma réplica do BERM e fontes radioativas de 137-Cs e 90-Sr. Os dados da calibração com protões de 2014 foram reanalisados. Foi criado e implementado um novo modelo do cross-talk nas funções de resposta do BERM. Os resultados foram convoluídos com diferentes modelos de radiação durante o flyby da Terra e comparados com o instrumento Solar Intensity X-Ray and Particle Spectrometer (SIXS), abordo da mesma missão, para validação. O modelo foi bem sucedido em reproduzir os canais de baixas energias de eletrões. A reconstrução dos fluxos em Solar Energetic Particles (SEP) com a bow-tie foi também validada com dados do SIXS.

Palavras Chave

BepiColombo; BERM; Eletrões; Protões; Eventos Solares; Mercúrio.

Contents

List of Figures

List of Tables

Acronyms

ADC Analogue-to-Digital Converter

ASIC Application Specific Integrated Circuit

BERM BepiColombo Environment Radiation Monitor

EQM Engineering Qualification Model

ESA European Space Agency

FPGA Field-Programmable Gate Array

GCR Galactic Cosmic Rays

GPE Gradual Proton Event

HEP-ion High-Energy Particle instrument for ion

IFE Impulsive Flare Events

JAXA Japan Aerospace Exploration Agency

LUT Look-Up Table

MGNS Mercury Gamma-Ray and Neutron Spectrometer

MPO Mercury Planetary Orbiter

MMO Mercury Magnetospheric Orbiter

MESSENGER Mercury Surface, Space Environment, Geochemistry and Ranging

MTM Mercury Transfer Module

SEP Solar Energetic Particles

SIXS Solar Intensity X-Ray and Particle Spectrometer

SIXS-P Particle detector of SIXS

SPM Solar Particle Monitor

1

Introduction

Contents

The space radiation environment can cause component and material deterioration, electrical malfunctions or even component loss. Continuous monitoring of the radiation environment is therefore essential to diagnose and if possible avoid anomalies and extend the lifetime of space missions. The BepiColombo Environment Radiation Monitor (BERM) is the instrument aboard the BepiColombo mission to Mercury, that has the task of monitoring the radiation environment [1]. BERM was developed by the European Space Agency (ESA) in cooperation with the Portuguese company EFACEC. It was designed to detect high fluxes of electrons with energies from ~100 keV to ~10 MeV, protons with energies from 1 MeV to ~200 MeV, and heavy ions with a Linear Energy Transfer from 1 to 50 MeV/mg/cm^2. Even though BERM is a housekeeping instrument, it is also provides relevant scientific information about the radiation environment.

1.1 BepiColombo Mission

BepiColombo is a joint mission between the ESA, and the Japan Aerospace Exploration Agency (JAXA) to explore Mercury [2, 3]. It consists of two spacecraft, Mercury Planetary Orbiter (MPO) from ESA and Mercury Magnetospheric Orbiter (MMO) from JAXA. Both share the same propulsion system, the Mercury Transfer Module (MTM). The mission was launched in 2018 and will enter Mercury's orbit in December 2025. During cruise, it will perform nine gravity-assisted flybys. The first flyby, was of the Earth in 2020. The second and third of Venus, in 2020 and 2021, and the others of Mercury between 2021 and 2025. The propulsion system will separate from the spacecraft after orbital insertion. The mission nominal end is planned to May 2027, but it can be extended for one additional year. The complete mission schedule is presented in table 1.1.

BepiColombo is only the third spacecraft to visit Mercury, after NASA's Mariner 10 that flew past Mercury three times between 1974-1975 [4] and Mercury Surface, Space Environment, Geochemistry and Ranging (MESSENGER) that orbited Mercury for more than four years from 2011 to 2015 [5]. BepiColombo will study Mercury in a unique configuration with one spacecraft orbiting close to the planet, MPO, and the other, MMO, outside the magnetosphere. The MPO spacecraft comprises 11 instruments listed in table 1.2.

1.1.1 BERM in the BepiColombo Mission

The MPO carries BERM to measure the environmental radiation levels during the cruise and nominal mission at Mercury. Complementary observations of the radiation environment, will be performed by a few other instruments onboard BepiColombo. These are the Solar Intensity X-Ray and Particle Spectrometer (SIXS) [7], the Mercury Gamma-Ray and Neutron Spectrometer (MGNS) onboard MPO [8],

Date	Event
20 0ctober 2018	Launch
10 April 2020	Earth flyby
15 October 2020	First Venus flyby
10 August 2021	Second Venus flyby
1 October 2021	First Mercury flyby
23 June 2022	Second Mercury flyby
20 June 2023	Third Mercury flyby
5 September 2024	Fourth Mercury flyby
2 December 2024	Fifth Mercury flyby
9 January 2025	Sixth Mercury flyby
5 December 2025	Mercury orbit insertion
14 March 2026	MPO in final science orbit
1 May 2027	End of nominal mission
1 May 2028	End of extended mission

Table 1.1: BepiColombo Mission Schedule.

and the High-Energy Particle instrument for ion (HEP-ion) and Solar Particle Monitor (SPM) onboard MMO [9].

BERM is placed on the radiation panel of MPO pointing away from the Sun, -Y axis (figure 1.1 show the representation of the reference frame). It will monitor the radiation environment, and for that reason, it will be operating continuously during the entire mission. During cruise, the scientific instruments will be turned only for specific calibration and science observation campaigns.

Despite being a housekeeping instrument, BERM can perform scientific investigations, more specifically of the interplanetary and Hermean environments:

- Characterising the Hermean radiation environment.
- Investigating the trapped and/or quasi-trapped particles in the Hermean magnetosphere.
- Characterising the properties of Solar Energetic Particles (SEP) close to the Sun.
- Studying the impact of space weather at Mercury, namely the effects of energetic particles bombardment (SEP and Galactic Cosmic Rays (GCR)) in the magnetosphere, exosphere and surface.
- GCR modulation in the inner solar system
- Study interplanetary physics under different conditions of the solar activity. The mission coincides with an ascending phase of the solar cycle.

During the Earth flyby, BERM measured the Earth radiation belts and particle background. This radiation environment is very well study, consisting in a good opportunity to calibrate and validate BERM response functions. It is also a great opportunity to cross-calibrate BERM with different instruments aboard BepiColombo and on other Earth missions. For this purpose, the most important instrument is the Solar Intensity X-ray Spectrometer (SIXS)-P. SIXS measures electron and proton energies partially overlapping with BERM's own measuring capabilities as it can be seen in Table 1.3. [1] [7]. Observations made with SIXS-P and BERM during the Earth flybys are used to validate the results obtained in this thesis.

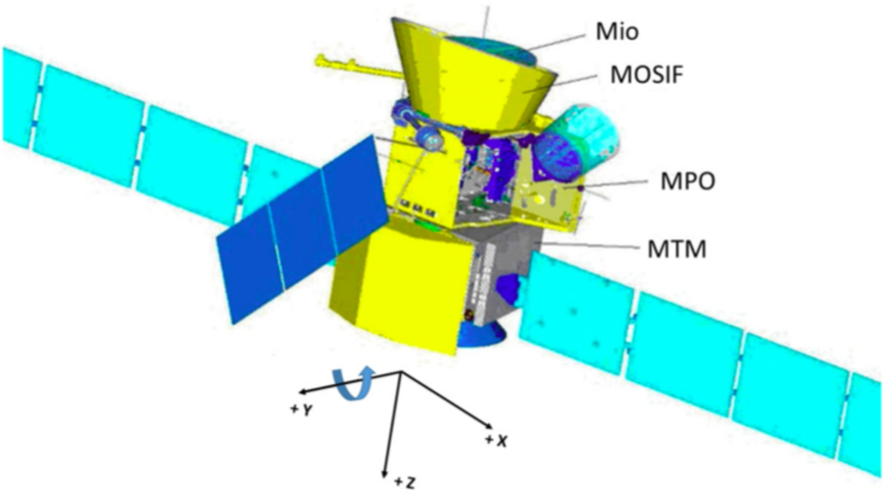

Figure 1.1: The composition of the spacecraft during cruise phase and its reference frame XYZ. [2]

1.2 Thesis Outline

This thesis was developed following [1] and [10]. At the beginning of this thesis, the first BERM response functions had already been computed and a bow-tie algorithm successfully implemented to convert channel count rates to particle flux. However, there were still a number of shortcomings. The first electron channel for example was unreliable indicating that the threshold for detection, calculated in [1], was not correct and/or that the cross-talk found in the same work needed to be implemented in the response functions. In this work, I analysed both characteristics of the detector, the threshold, and the crosstalk. I performed radioactive source tests to the BERM spare instrument to obtain the threshold and to model the crosstalk. The results were validated successfully using flight data.

This thesis is organised in six chapters. The second chapter has a description of the environment that the mission will encounter, providing some key information about particle sources, energies, and fluxes. The third chapter provides a complete description of BERM. The main characteristics and results of this instrument, described in [1, 10], are presented in this chapter. The motivation for this work is also explained in-depth. The Fourth chapter presents the complete analysis performed during this thesis and the results obtained. The fifth chapter shows the validation of the BERM model produced in this thesis, using the Earth flyby and SEP data. The conclusions are presented in the sixth chapter and the future steps are discussed.

Instrument		Observational Objective
BELA	BepiColombo Laser Altimeter	Characterize the topography and surface morphology of Mercury.
MORE	Mercury Orbiter Radio Science Experiment	Determine Mercury's gravity field as well as the size and physical state of its core.
ISA	Italian Spring Accelerometer	Study Mercury's interior structure and test Einstein's theory of relativity.
MPO-MAG	Mercury Magnetometer	Describe Mercury's magnetic field and its source.
MERTIS	Mercury Thermal Infrared Spectrometer	Determine Mercury's mineralogical composition and obtain a global map of the surface temperature.
MGNS	Mercury Gamma-ray and Neutron Spectrometer	Determine the elemental composition of Mercury's surface distribution of volatiles in the polar areas.
MIXS	Mercury Imaging X-ray Spectrometer	Obtain a global map of the surface atomic composition.
PHEBUS	Probing of Hermean Exosphere by Ultraviolet Spectroscopy	Characterize the composition and dynamics of Mercury's exosphere.
SERENA	Search for Exosphere Refilling and Emitted Neutral Abundances	Study the interactions among the surface, exosphere, magnetosphere, and the solar wind.
SIMBIO-SYS	Spectrometers and Imagers for MPO Integrated Observatory System	Provide global, high-resolution, and infrared imaging of the surface.
SIXS	Solar Intensity X-ray and particle Spectrometer	Perform measurements of solar X-rays and energetic particles at high time resolution.

Table 1.2: Instruments on the BepiColombo Mercury Planetary Orbiter, MPO. [6]

Instruments	Electron Energy Range	Proton Energy Range	Heavy Ions
BERM	0.1 - 10 MeV	1 - 200 MeV	1 - 50 MeVmg^{-1}cm^{-2}
SIXS	0.05 - 3 MeV	1 - 30 MeV	—

Table 1.3: BERM and Particle detector of SIXS (SIXS-P) detection ranges.

2

Space Radiation Environment

Contents

Due to its small distance from the Sun (presented in table 2.1), Mercury has a unique environment in the Solar System. It is also the only solid body in the inner Solar System besides Earth to possess a (weak) global magnetic field. These two characteristics combined allow the planet to support a small and dynamic magnetosphere of significant scientific interest [2, 3]. It is this unique interaction between the Sun radiation and the Mercury magnetosphere that motivates the BepiColombo mission. Another key investigation is the impact of Galactic Cosmic Rays (GCR) and Solar Energetic Particles (SEP) in Mercury's surface. [2, 3].

Parameters	Earth	Mercury
Sun Distance (AU)	1	0.31-0.47
Sidereal orbital period (Earth's day)	365.26	87.97
Rotation Period (Earth's day)	1	58.6
Radius (km)	6371	2440
Mass (10^{24} kg)	5.97	0.33
Density (gcm^{-3})	5.5	5.4
Magnetic Field moment	31000 nT R_E^3	195 nT R_M^3
Inclination of magnetic axis to rotation axis (°)	11	0

Table 2.1: Mercury's and Earth's parameters. Adapted from [3]

2.1 Solar Particles

2.1.1 Solar Winds

From the outer region of the Sun, there is a continuously emission of charge particles, also known as the solar wind. These particles, are ejected from the corona (outer layer of the sun), where the gravitational force of the sun can no longer hold them. The solar wind is composed of electrons, ions, alpha particles and heavier nuclei that are ejected from the Sun, creating a large region around it called the heliosphere. In the case of Mercury, at such a short distance from the Sun, these particles can have velocities from 250 - 650 Km/s with densities of 15-105 particles/cm^{-3}, as presented in table 2.2 [3, 11].

Parameters	Earth	Mercury
Sun Distance (AU)	1 AU	0.31-0.47 AU
Solar wind speed (km/s)	320-710	250-650
Solar wind density (cm^{-3})	3.2-20	15-105
Proton temperature (10^4 K)	8	13–17
Interplanetary magnetic field (nT)	6	31$\pm$ 11

Table 2.2: Solar wind typical values at Mercury and at Earth. Adapted from [3]

Despite the large range of solar wind speeds, the average value of 430 km/s does not change much with distance. The most significance difference that can be seen, is in the solar wind density, that is much higher in Mercury than at Earth.

2.1.2 Solar Energetic Particles

Besides the solar wind, there are sporadic events such as Solar Flares and Coronal Mass Ejections that emit Solar Energetic Particles (SEPs) with different characteristics [12]. These events consist of large fluxes of high energetic electrons, protons and heavy ions up to Iron (z=26), accelerated to energies in the keV-GeV range [13]. SEP events are usually divided in two different groups: Impulsive Flare Events (IFE) that are energetic particles accelerated at the base of the solar corona in association with flare eruptions; and Gradual Proton Event (GPE) that are energetic particles accelerated by coronal mass ejection, up to several solar radii [14] .

Both events are composed mainly of protons, but also electrons and heavy ions. However they differ in terms of charge state, spatial and temporal distributions and flux intensities. IFE have lower fluxes but are much more frequently, being detected on Earth 100 times per year, while GPE occur only about 10 times during the Solar maximum. In terms of duration, GPE can last up to 2-3 days, while IFE only last few hours.

While each SEP event can vary significant, the profile of both types can be portrayed with the same features as shown in figure 2.1. Their general properties are [12]:

- **Propagation Delay** - It is the time delay between the event onset and the increase of particle fluxes.
- **Intensity Rise** - When the particle flux starts to increase, there is a rapid rise to a maximum which typically takes 1-3 hours but may extend to several hours. Initially it has an an-isotropic flux, favouring the direction of the Sun, but gradually becoming more isotropic [12].
- **Decay** - Slow decay to the background level (essentially exponential decay, typically dropping 1/e within 10 to 14 hours).
- **Flux Enhancement** - The event can include short periods of flux enhancement, as a fast and powerful interplanetary shock passes over the observer.

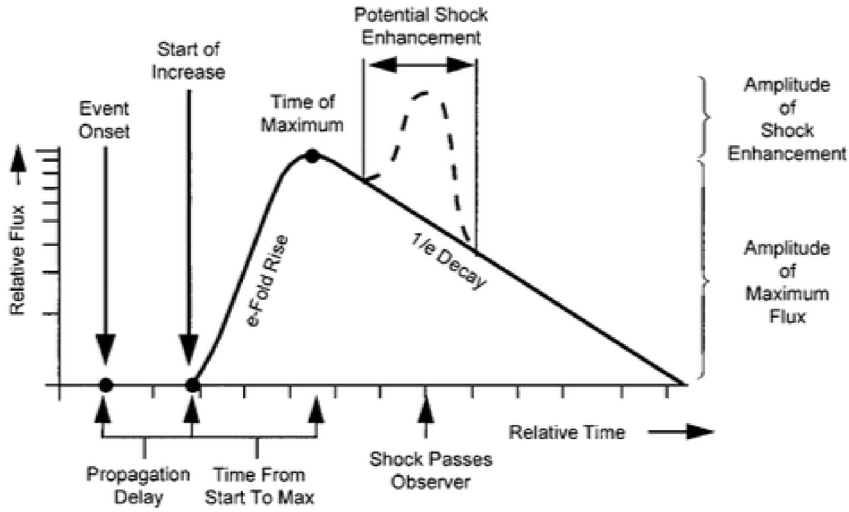

Figure 2.1: Idealised SEP profile. [12]

2.2 Galactic Cosmic Rays

GCR are highly energetic particles accelerated in our galaxy to energies from 10^9 eV up to 10^{17} eV. GCR consist mainly of protons (90%), nuclei and ions. Because of their constant flux and highly energetic range, GCR are an important part of the radiation environment in interplanetary space and at Mercury. GCRs interact with the Hermean surface and exosphere, modifying it, and producing secondary particles such as gammas and neutrons that can be used to study the planet's composition [3]. One of the main scientific goals of BepiColombo is to evaluate the effects of GCR in the Hermean radiation environment. GCR flux is affected by solar activity, that creates a magnetic cutoff for charged particles. The flux is anti-correlated with solar activity, i.e., the GCR flux is higher during the solar minimum and lower during solar maximum. BepiColombo's cruise will encounter both solar maximum and solar minimum conditions, allowing to study GCR modulation in the inner Solar System during this period [3].

2.3 Earth Radiation Belts

The Earth is the other planet in the inner Solar System to have a global magnetic field and as consequence, a magnetosphere. In the region of the space, around the planet , the magnetic field can exert influence on charged particles. This influence can cause deflection of the particles path, preventing them to hit a planet and/or trap charge particles along its magnetic field lines, creating belts of radiation around the planets, in a shape of a torus. Radiation belts are known to exist on the Earth since 1958 [15], but have also been found on Jupiter, Saturn, Uranus and Neptune [16].

The Earth has two radiation belts, the Van Allen belts, represented in figure 2.4. This belts consist mainly of electrons and protons produced by SEPs and by the interaction of GCR with the atmosphere. The inner belt is mainly composed of protons with energies that can exceed 100 MeV, and an extension of 1 to 3 Earth radius measured in the equatorial plane. The outer belt is mainly composed of electrons, with energies up to 10 MeV, and an extension from 4 to 7 Earth radius. Between the two radiation belts there is a region with low flux of trapped particles, the slot region [17, 18].

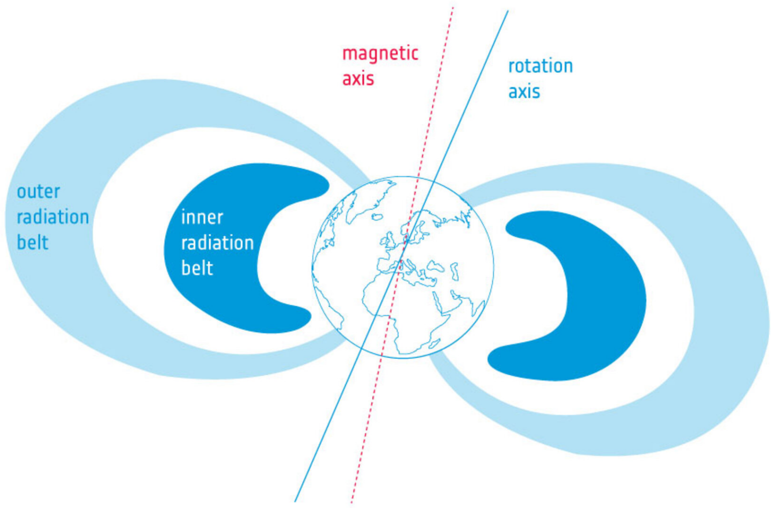

Figure 2.2: Representation of the two Earth radiation belts [19].

2.4 Mercury Magnetosphere

The magnetosphere of Mercury represents a important subject of study, mainly because of it's unique characteristics. In the Solar System, Earth and Mercury are the only terrestrial planets with a global magnetic field that gives rise to a magnetosphere. In the case of Mercury, the magnetic field moment is much lower and the planet is much closer to the Sun, creating a complete different scenario in terms of interaction of the solar events with the magnetosphere. At such a close distance to the Sun, solar wind pressure and interplanetary magnetic field are typically one order of magnitude higher than at one astronomical unit.

Due to the magnetic field interaction with the solar wind, the magnetosphere is highly dynamic and it is composed of different regions, the magnetopause, plasma sheet and bowshock, as illustrated in the figure 2.3.

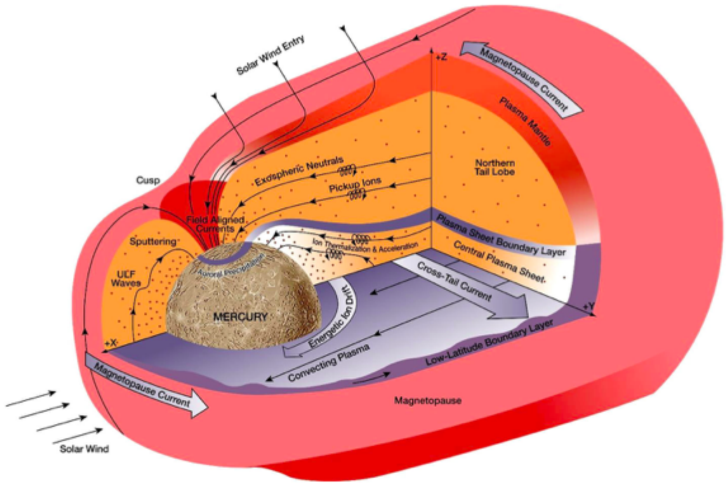

Figure 2.3: Schematic view of Mercury magnetosphere structure [20]

2.4.1 Mercury Electron Burst

In the first mission to Mercury, it was found quasi-trapped energetic electrons in Mercury's magnetosphere. These events are related to the dynamics of the magnetosphere of the planet, that is unable to trap energetic particles. However the reconnection and particles acceleration mechanisms at Mercury, is not yet established [2].

With Mariner 10 data, it was not possible to fully identify the species, flux or energy spectrum of these bursts. Mercury Surface, Space Environment, Geochemistry and Ranging (MESSENGER) determined that these electrons had an energy range of 30-300 keV [21]. It was also found that the energy distribution exhibits a significant drop above 100 keV. The bursts were detected with a time distribution between several minutes to nearly an hour [21, 22]. No ion was detected with energy above 35 keV. This was not very surprising, based on the weak Mercury's magnetic field.

These bursts are interpreted as being electrons accelerated by inductive electric field resulting from the rapid reconfiguration of the magnetic field [23]. This behaviour can be seen in the figure 2.4, where the dashed line indicates the sudden increase in the B_Z magnetic field, between the growth phase in the B_X magnetic field and the peak of electron detection. Due to the transient configuration of the events and their small time scale, these particles do not complete a full orbit around the planet in the azimuthal direction before being lost. Consequently there is no "Van Allen"-like radiation belts, as it is seen in other planets with an internal magnetic field.

BepiColombo as already perform 3 Mercury flybys, in which BERM did not detect any event.

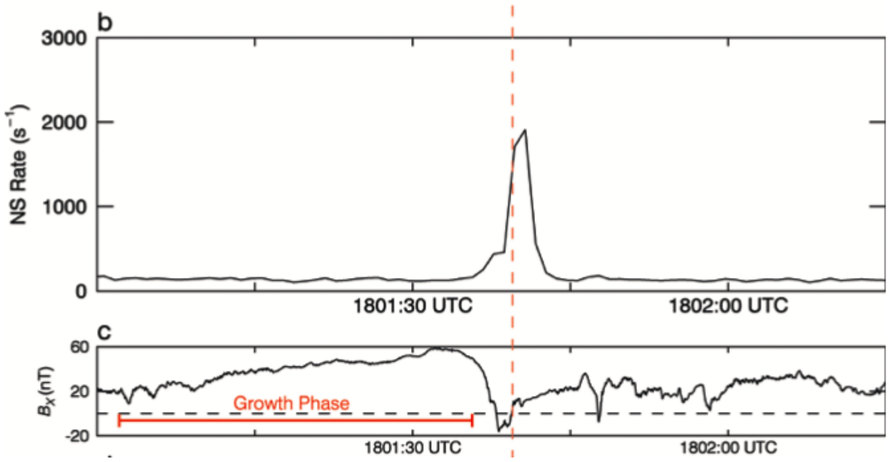

Figure 2.4: An electron burst event detected by the Neutron Spectrometer (NS) of MESSENGER mission, sensitive to electrons (top), B_X magnetic field, displaying an one minute growth phase, before the burst. The vertical dashed line marks the sudden increase in the BZ magnetic field coordinate [23]

3

The BepiColombo Radiation Monitor

Contents

BepiColombo Environment Radiation Monitor (BERM) is an energetic particle detector composed of 11 silicon detectors with areas from 0.5 mm^2 to 903 mm^2, and thickness of 0.3 mm, with the exception of the first detector which is 0.2 mm thick. Between the silicon layers there are absorber layers, to reduce the energy of the incident particles, composed of aluminium and tantalum, with a thickness from 0.5 mm in the first layer, up to 1.5 mm in the last layer. All these components are inside an aluminium box, with tantalum shield walls, with 2.143 kg and 174.8 $\times$ 120.0 $\times$ 107.0 mm^3. The collimator is made of tantalum and provides a $40°$ field-of-view and a 25 μm thick beryllium layer to cut-off low energy electrons ($<$ 50 keV) and protons ($<$ 1.35 MeV) [1]. All these components can be seen in BERM´s side view in figure 3.1. BERM energy ranges and resolution are presented in table 3.1 for electrons, protons and heavy ions.

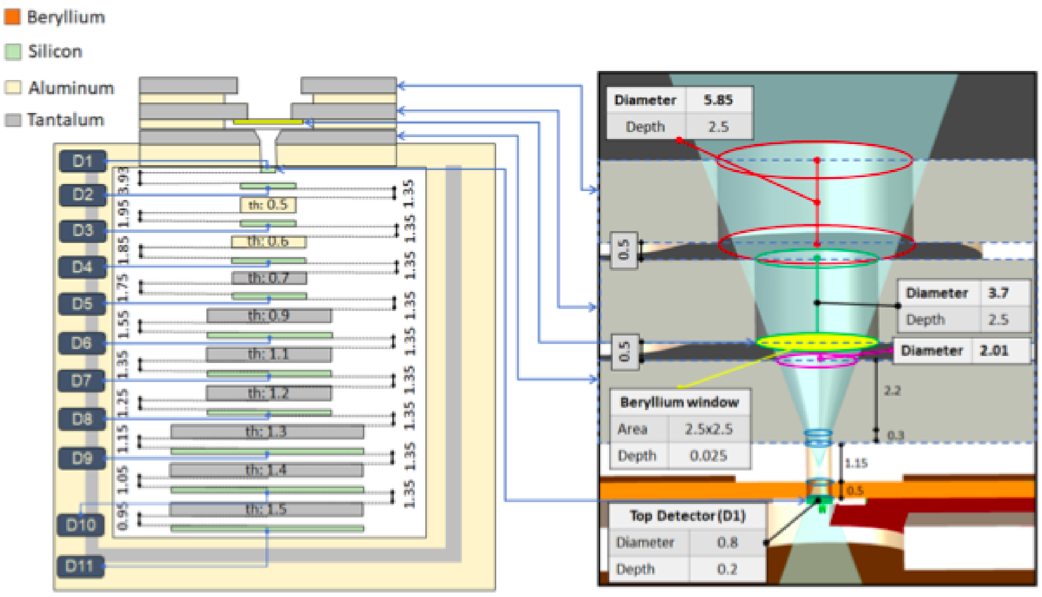

Figure 3.1: Side view of the BERM physical concept with the 11 silicon detectors, the tantalum collimator and the side and bottom shielding (left). Top view of BERM's collimator (right). All units are in millimeters. D1 corresponds to the first detector, D2 to the second etc. [1]

Species	Energy (MeV)	Resolution (# of channels)
Electron energy	$\sim$ [0.15 ; 10]	5
Proton energy	$\sim$ [1.5 ; 100]	8
Heavy Ion energy	$\sim$ [1 ; 50] /(mg·cm^2)	5

Table 3.1: BERM particle energy ranges and resolutions

3.1 Working Principle

BERM was designed to detect charged particles, measure their energy, and distinguish their species, namely electrons, protons, and heavy ions. This is done based on two principles: how deep in the stack a particle has travelled, and how much energy it has deposited. The particles lose energy at different rates both in the detector and in the absorber layers. This means that different particles generate different deposited energy patterns in the silicon stack.

3.1.1 Interaction of Particles with Matter

Charged particles crossing a material interact with the electrons and nuclei in matter, losing energy in the process. This energy loss is mainly due to excitation and ionization of atoms, and is dependent both on the incoming species and energy, and the material that is being crossed. In the energy ranges considered, this interaction is described by the Bethe-Bloch formula (eq 3.1), that models the average energy loss of incoming particles per unit of distance (-dE/dx), also known as the stopping power of the material. Usually this quantity is used normalised to the material density, as presented in equation 3.1.

$$\frac{-1}{\rho}\frac{dE}{dx} = K\frac{Z}{A}\frac{z^2}{\beta^2}\left[ln\left(\frac{2mc^2\beta^2\gamma^2T_{up}}{I^2}\right) - \beta^2\left(1+\frac{T_{up}}{T_{max}}\right) - \delta - \frac{2C_e}{Z} + F\right] \tag{3.1}$$

$$K = 2\pi N_a r_e^2 m_e c^2 \tag{3.2}$$

Where r_e^2 is the classical electron radius, m_e is the electron rest mass, N_a is the Avogadro's Number, ρ is the material density, z is the incoming particle charge, A is the material mass number, I is the mean excitation of material, Z is the atomic number of material, C_e is the shell correction function, F represents higher order corrections, δ is the density effect function and T_{max} is maximum transfered energy in the collision. The values $\gamma = E/mc^2$, $\beta = 1 - \frac{1}{\gamma^2}$ and $T_{up} = max(T_{cut}; T_{max})$.
As it can be seen in figure 3.2, in the energy range of BERM, electrons have a different behaviour from protons and alpha particles. At these energies, electrons are minimum ionising particles (MIP), which means that, their stopping power does not change significantly. Protons and alpha particles stopping power vary with incoming particle energy. For these two particles, the stopping power is inversely proportional to the energy, meaning that the lower the energy of the incoming proton or alpha particle, the higher the energy deposited in the detector. From figure 3.2 we can also see that, in the energy range of BERM, alpha particles deposit more energy, in silicon, than protons, which in turn deposit more energy than electron. This principle is the basis of the particle distinction done by BERM. Figure 3.2, shows the mean value of the stopping power of silicon, however, this quantity is associated to a distribution, which means that the energy deposited by high energetic protons and low energetic electrons may overlap.

This means that these particles might be misidentified as the other - contamination.

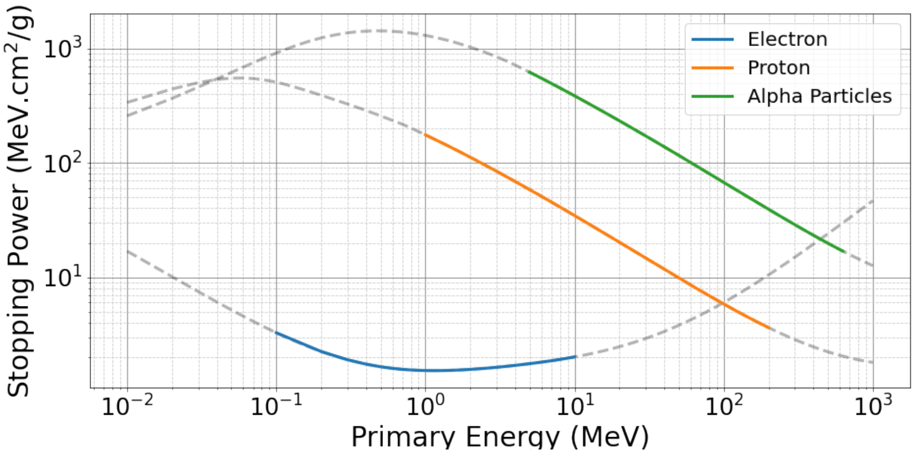

Figure 3.2: Total stopping power of silicon for electrons, protons and alpha particles. The thick line represents the energy ranges of BERM. The plots were made based on the values of the Bethe's formula, taken from the web-based ESTAR [24], PSTAR [24] and ASTAR [24] databases provided by NIST: National Institute of Standards and Technology.

3.2 Detectors

BERM is composed of 11 Passivated Implanted Planar Silicon (PIPS^{TM}) solid-state semiconductor detectors from Camberra. A silicon detector is designed to detect charged particles that cross the material. This is obtained with a PN junction, that consist of two doped silicon layers put together. One of the silicon layers is doped with a material with less than four valence electrons (acceptor material or P layer) and the other with a material with more than four valence electrons (donor material or N layer). Together the number of valence electrons must sum up to eight [25]. This type of device has two main characteristics, a small energy gap, typically $E_G \approx 1$eV, due to the semiconductor material that is in the base of the both layer, and a depletion region. The last one is caused by the doped materials. The N type layer have an excess of valence electrons and the P type layer have a deficit (named holes). This will make the electrons cross from the N type layer to the P type layer, creating a diffuse potential between them. This potential is amplified with an applied external negative potential (50V in the case of BERM), causing the entire device to be fully depleted.

In this regime of operation, a charge particle crossing the material will interact with it, creating a electron-hole pairs, which leads to a current. This current is proportional to the energy deposited by the particle. To form an electron-hole pair takes in average 3.6 eV in silicon. [26, 27]

3.3 Signal Processing

Signal processing in BERM is done in three steps, event profile energy reconstruction, event validation and the particle identification, resulting in the attribution of events to channel, as presented in figure 3.3. BERM has four modes of operation, the idle mode, the spectral mode, the test backend mode and the test frontend mode, and depending on the mode of operation, some of the steps can be omitted. In spectral mode and in both test modes, the output is a histogram with 20 channels. First channel has the total number of triggered events, followed by five channels for electrons, eight for protons and five for heavy ions. The last channel has the number of unidentified events, by the particle identification algorithm. Idle mode has 14 channels, where channels 2-12 are directly connected to the 11 detectors. The output of this mode is the energy deposited in each detector for all events in Analogue-to-Digital Converter (ADC) units.

During most part of the mission BERM is in Spectral mode, and the signal passes through the three processing steps. This mode separates the events in channels, depend on there type and energy. In this mode, particle type and energies are separated using an algorithm that analyses their deposited energy pattern and energy thresholds, stored in a Look-Up Table (LUT). Test backend uses as input a file with energy, in ADC, deposited in all detectors and only performs the particle identification process. Test frontend uses as input an electrical signal simulating the output of each detector, generated internally by BERM. The signal passes through all steps of the on-board signal analysis. In idle mode no signal processing is performed.

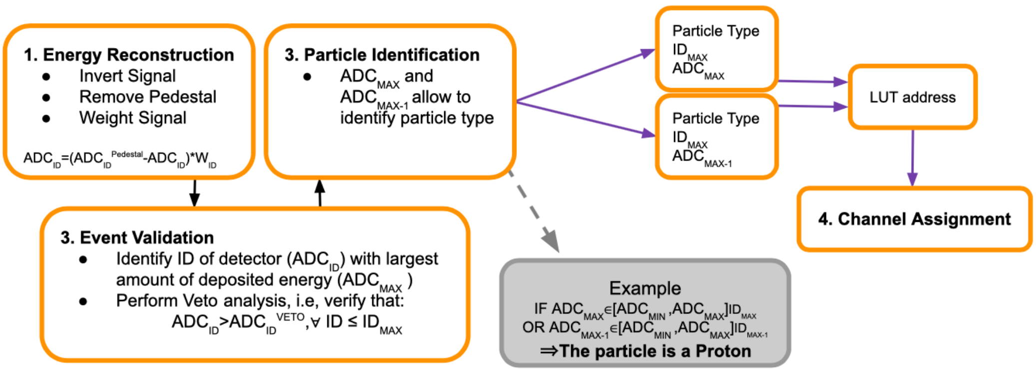

Figure 3.3: Representation of the steps of the signal processing (adapted from [1]).

3.3.1 Signal Acquisition and Energy Reconstruction

The output of the silicon detectors, is an electrical signal that is converted into a 14 bit ADC word. For this purpose, the electrical signal produced by the silicon detectors is read by a dedicated VA32TA2.2

Application Specific Integrated Circuit (ASIC) presented in figure 3.4, developed by IDEAS(datasheet obtained per request from www.ideas.no).

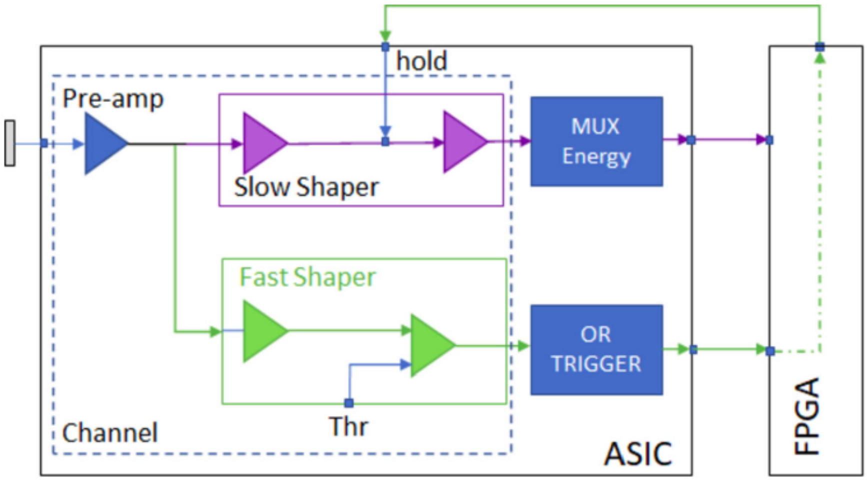

Figure 3.4: Representation of VA32TA2.2 ASIC, responsible for reading the detector's signal in BERM, and converting in to a digital signal with 14 bits. [1]

Each BERM detector is connected to an ASIC channel, composed of two units, as represented in the figure 3.4, the VA and the TA units, in to which the signal is split after being amplified. The VA unit is composed of a slow shaper that integrates the signal in 2 μs and is then read by an analogue multiplexer, that converts the signal into the 14 bit format. In the slow shaper, there is also an hold unit whose the activation depends on the response of the TA unit. The TA unit has a fast-shaper, that will rapidly (75 ns) integrate the signal and compare it with a programmable trigger threshold. If the signal is above the threshold, the signal in the VA unit is read by the analogue multiplexer, triggering the event, otherwise the event is rejected. In BERM only the first detector is used to triggering the events. The connection between the TA unit and the hold unit is done by the on-board Field-Programmable Gate Array (FPGA). The slow shaper has a 10 μs discharge time, that limits the read out to 100kHz. The 14 bit digital signal is defined with 0 corresponding to the maximum value, and a null signal in the detector corresponding to 16384 ADC units.

The signal obtained in ADC units for each detector is processed in a FPGA in three steps. First, the signal is inverted, in order to have 0 corresponding a null signal, and 16384 ADC corresponding to the maximum value. Second, the pedestal is removed - the pedestal is a characteristic of each detector and correspond to the electronic noise present even when no particle is crossing the detectors. The third step is a correction to the signal due to the fact that different detectors have different sizes, and consequently different capacitance. This step is necessary because the signal is read simultaneously in all detectors. A detector with large capacitance will produce a signal, that takes longer to reach the maximum value. For that reason, a weight factor is applied with the objective of obtaining the correct signal amplitude at the peak. The result is a digital signal, in ADC, corresponding to the energy deposited in the detectors. To convert to energy in MeV, it must be applied the conversion coefficient from ADC to MeV.

The pedestal, weight and conversion coefficients were obtained in the ground calibration of BERM [1], and the results are presented in table 3.2. The pedestal and weight coefficients were stored in the BERM's LUT. The BERM trigger threshold value, obtained with the ground calibration data is 220 keV, with a standard deviation of 24 keV. This parameter can be changed, in a nominal scale of -15 to 15, and is currently set at 0. All values stored in the BERM LUT are programmable.

Detector ID	1	2	3	4	5	6	7	8	9	10	11
Radius(mm)	0.4	4		6.9		11.95			16.95		
Thickness (mm)	0.2	0.3									
Zero (ADC)	1504	1575	1598	1473	1399	1498	1606	1456	1398	1551	1543
Weight	1			1.2					1.4	1.6	1.8
Veto (ADC)	8					12			32		NA
ADC to MeV coefficient (ADC/MeV)		1098.10	1198.30	1136.20	1204.80	975.31	958.49	931.27	826.31	807.05	855.06

Table 3.2: BERM detectors specifications. [1]

3.3.2 Event Validation

Event validation starts by finding the detector (ID_{MAX}) where the largest amount of energy was deposited (ADC_{MAX}). Then, a veto analysis is performed with the objective of eliminating events that were not produced by a particle entering the collimator aperture. In this analysis, the ADC_{MAX} value and the values deposited in the preceding detectors are compared with the Veto values (table 3.2) attributed for each detector. Only if all of preceding detectors have a deposited energy above these values, the analysis proceeds.

3.3.3 Particle Identification Algorithm

The particle identification algorithm is performed with energy selection thresholds (presented in the table 3.3) applied to each non-vetoed event. The signal of the ID_{max} (and $ID_{max\text{-}1}$ for all detectors except the first) is compared with the values of the table 3.3, and attributed a 17 bit address. These bits contain information regarding the particle type, the detector with larger deposited energy and a selection of 11 bits of the signal measured in the detector that precedes it (see figure 3.5). So for the first detector, there is only one energy to consider (kADCn), and in this case if kADCn $<$ 349 the event is an electron, if 349 $<$ kADCn $<$ 5999 the event is a proton and if kADCn $>$ 5999 the event is an heavy ion. For the other detectors, the process follows the same logic, but with two energies to take in consideration (kADCn and kADCn1). So for ID_{max}>1 the order is important. First, the algorithm checks if the event is a heavy ion, then if it is a proton and last if it is an electron. To be consider an heavy ion kADCn $>$ 5999 or kADCn1

$>$ 4999, a proton 349 $<$ kADCn $<$ 5999 or 280 $<$ kADCn1 $<$ 4999 and an electron kADCn $<=$ 349 or kADCn1 $<=$ 279. The energy deposited attributed to the event, is the kADCn1 (and kADCn for ID_{max}=1). The LUT address with the same value contains the channel value to which the particle is assigned.
Every detector is assigned to only one channel of each particle type with the exception of the first, which is connected with two electron channels, and the second detector that is connected to two proton channels (see table 3.4). In the first case, if the events is considered a electron and has ID_{max}=1, the energy deposited in the first detector is used to distinguish between channel 1 and 2, using the selection threshold presented in table 3.3. In the second case, if the events is considered a proton and has ID_{max}=2, the energy deposited in the first detector (ID_{max-1}) is also used to distinguish between channel 7 and 8, using the selection threshold presented in the same table.
There is one last exception to the particle identification algorithm. If an event have $ID_{max}>1$, and kADCn$<$350 or kADCn1$<$280, one more criteria is applied to the algorithm:

$$\text{If} \quad \text{coef. x kADCn1} > \text{kADCn} \quad \text{—>} \quad \text{Proton} \tag{3.3}$$

$$\text{Otherwise} \quad \text{—>} \quad \text{Electron} \tag{3.4}$$

The coefficient used in the inequality 3.4 is programmable, being now set at 1.075. This exception is important to distinguish electrons and protons with similar deposited energies, but different deposition pattern.

<table>
<tr><th>Detector</th><th colspan="2">kADCn</th><th colspan="2">kADCn1</th></tr>
<tr><td>Unit</td><td>ADC</td><td>MeV</td><td>ADC</td><td>MeV</td></tr>
<tr><td>$Th^{electrons}_{max}$</td><td>349</td><td rowspan="2">0.29 - 0.43</td><td>279</td><td rowspan="2">0.23 - 0.35</td></tr>
<tr><td>$Th^{protons}_{min}$</td><td>350</td><td>280</td></tr>
<tr><td>$Th^{protons}_{max}$</td><td>5999</td><td rowspan="2">4.98 - 7.43</td><td>4999</td><td rowspan="2">4.15 - 6.20</td></tr>
<tr><td>$Th^{heavy\ ions}_{min}$</td><td>6000</td><td>5000</td></tr>
<tr><td>Th^{ch1}_{max}</td><td>127</td><td rowspan="2">0.11 - 0.18</td><td>—</td><td>—</td></tr>
<tr><td>Th^{ch2}_{min}</td><td>128</td><td>—</td><td>—</td></tr>
<tr><td>Th^{ch7}_{max}</td><td>—</td><td>—</td><td>1599</td><td rowspan="2">1.33 - 1.98</td></tr>
<tr><td>Th^{ch8}_{min}</td><td>—</td><td>—</td><td>1600</td></tr>
</table>

Table 3.3: Selection threshold values applied to each detector to distinguish the channel that the event will be attributed to.

3.4 BERM Response Function

It is impossible to fully characterize a space radiation monitor on Earth. The space radiation environment is composed of different types of particles with energies spanning multiple orders of magnitude, with

ID_{max}	Channel																	
	1	2	3	4	5	6	7	8	9	10	11	12	13	14	15	16	17	18
1	X	X				X								X				
2			X				X	X						X				
3			X						X						X			
4				X						X					X			
5				X							X					X		
6					X						X					X		
7					X							X					X	
8					X							X					X	
9													X					X
10													X					X
11													X					X

Table 3.4: Relation between detectors and channel.

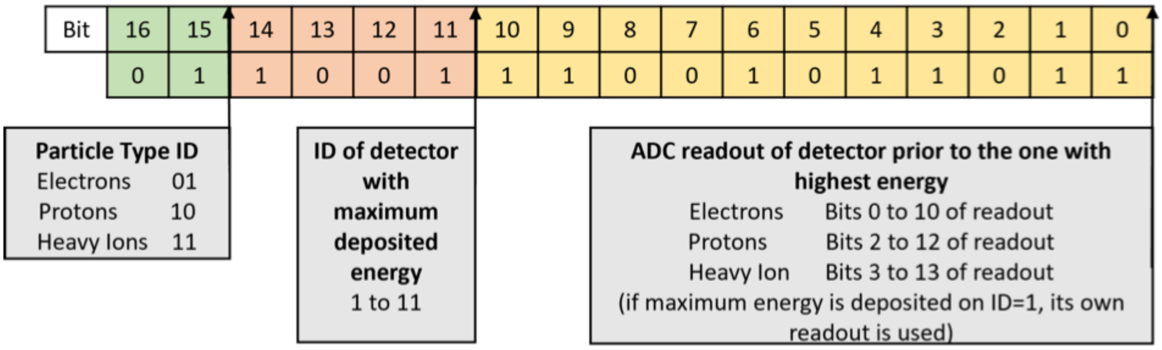

Figure 3.5: Energy reconstruction LUT address schematic. [1]

fluxes, for the most part, omni-directional. To obtain the BERM response functions, extensive Geant4 [28] - the most widely used particle transport tool - simulations were performed. Using this method, it is possible to take in consideration all types of interactions between the incoming particles and the detectors. If a sufficient number of particles with different characteristics is simulated, the outcome is a statistical reliable description of the detector behaviour.

3.4.1 Geant4 Simulations

Geant4 (GEometry ANd Tracking) [28] is a toolkit to accurately simulate the interactions of particles with matter. The simulation includes all relevant aspects of the process:

- the geometry of the system
- the materials involved
- the fundamental particles of interest
- the generation of primary events
- the tracking of particles through materials and electromagnetic fields

- the physics processes governing particle interactions
- the response of sensitive detector components
- the generation of event data
- the storage of events and tracks
- the visualization of the detector and particle trajectories, and
- the capture and analysis of simulation data at different levels of detail and refinement

To simulate particle interactions with BERM, a detailed mechanical description of it, was converted from a STEP (Standard for The Exchange of Product Data) file to Geometry Description Markup Language (GDML), via GUIMesh [29] (see figure 3.6). A dedicated Geant4 application was built. This application simulates primary energetic particles and tracks them as they interact with the computational model of BERM. The tracking is done step by step, until the particle have a range lower than a cutoff (10μm for the simulations used in this work) or gets out of BERM boundaries. All physical processes are computed with well-established interaction cross sections implemented in the Geant4 toolkit. The particle source consists of a rectangular planar source with a 120$\times$123 mm^2 area. The angular distribution of the particles was considered to be isotropic, and their energy spectrum was assumed to follow an inverse power law, normalised to a flat energy spectrum in order to optimise the computation time.

The result of the simulation is a set of deposited energies in all detectors and the initial energy of the particle. The results are used as an input for BERM's algorithm, to reproduce its output for different incoming particles.

In this work, the results of the simulations done for [1] and [10] were used. The number of simulated electrons and protons and the respective energy ranges are given in table 3.5.

Files	Particles	Energy (MeV)	Number of Simulated Particles
E1PF.root	Electrons	0.1-2.0	18x10^9
E2PF.root	Electrons	2-10	5 x10^9
P1PF.root	Protons	0.1-2.0	7 x10^9
P2PF.root	Protons	2-10	10x10^9
P3PF.root	Protons	10-80	10x10^9
P4PF.root	Protons	80-150	1 x10^9
P5PF.root	Protons	150-250	1 x10^9
P5PF.root	Protons	250-1000	81x10^6

Table 3.5: Output files from Geant4 simulation analysis.

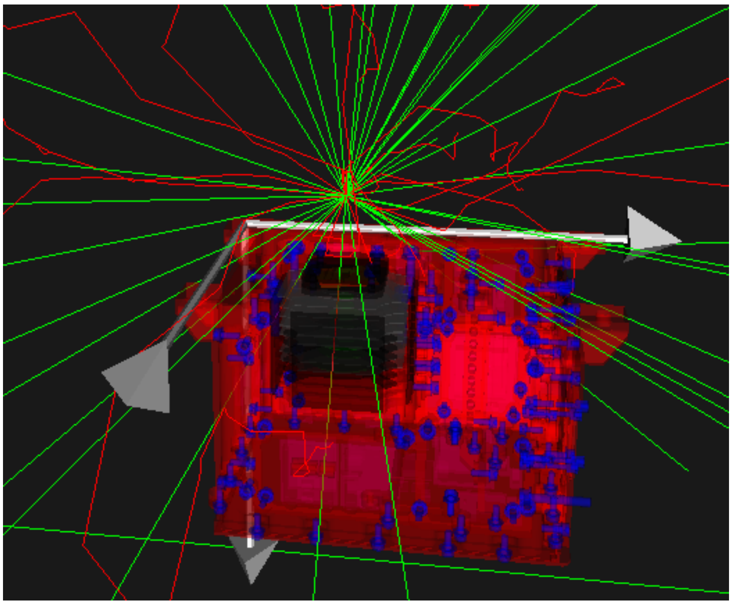

Figure 3.6: BERM representation in Geant4 simulation.

3.5 Electrons and Protons Response Function

To obtain the sensitivity of BERM's channels to incoming particles, the fraction of particles attributed to each channel in relation to those simulated needs to be computed. This is done with equation 3.5, that considers a source of area A and a hemispherical isotropic angular distribution around the surface normal to each dA of the source.

$$F_R(E) = A\frac{N_{channel}(E)}{N_{Inc}(E)} \int_0^{2\pi} d\phi \int_0^{\pi/2} sin(\theta)cos(\theta)\, d\theta = A\pi\frac{N_{channel}(E)}{N_{Inc}(E)} \tag{3.5}$$

Where $N_{channel}$ is the number of particles that were attributed to that channel, with energy E and N_{inc} is the total number of simulated particles with energy E.

When simulating the channels response function, it is important to take in consideration channel contamination. Despite the fact that each channel was design to detect a specific type of particle, all 18 channel have a non null sensitivity to any particle type that enters BERM. So instead of 18 response function, one for each channel, there are in fact, 18 for each type of particle. In this work, it will only be taken in consideration the ones with electrons and protons as incident particles. For electrons, the response function of the heavy ions channels (channels 14-18) is too low to take in consideration. In the electron energy range of BERM, is very unlikely that an electron deposit enough energy in a detector, in order to be consider an heavy ion.

BERM Flight Channels	1	2	3	4	5	6	7	8	9	10	11	12	13	14	15	16	17	18
Incident Protons	EP1	EP2	EP3	EP4	EP5	P1	P2	P3	P4	P5	P6	P7	P8	HP1	HP2	HP3	HP4	HP5
Incident Electrons	E1	E2	E3	E4	E5	PE1	PE2	PE3	PE4	PE5	PE6	PE7	PE8	–	–	–	–	–

Table 3.6: Response function nomenclature, depending on the incident particles and the channel.

3.5.1 Electron Response Function

Figures 3.7, 3.8 and 3.9 present the mean energy deposited by electrons in each detector as a function of energy and the electron response functions in electron and proton channels respectively. In figure 3.7, only particles that deposit energy in all detectors up to the one with the maximum deposited energy are considered. This condition avoids secondary particles that would change radically the functions without contributing for the analysis at this point. The first eight detectors are presented, because the last three are not associated to any electron channel. It is also shown the different selection thresholds for all the detectors. The BERM trigger threshold is also shown. The first four detectors have relatively similar response functions, with the following structure:

- **Starting Point** - The primary energy has to be high enough so that electrons reach the detector. The deeper the detector is in the stack, the higher the energy needed to reach the detector.
- **Calorimeter** - Growing in energy, the particle will stop in the detector leaving its entire energy there. The higher the primary energy, the higher the deposited energy. This creates a linear component in the mean deposited energy function, typical in calorimeters.
- **Peak** - At some point the particle will have enough energy to cross the detector and leave with some energy. The higher the primary energy, the more transparent the detector is to the particle and the mean deposited energy decreases. The position of the peak is dependent on the geometry of the detectors. For deeper detectors is in the stack, the primary energy of the particles needs to be higher, in order to start crossing the detector and leaving with some energy. Resulting in peaks with higher energies for detectors deeper in the stack.
- **Tail** - For higher electron primary energies, the mean deposited energy does not change significantly for all detectors in the stack.

One of the determining characteristics of BERM is the trigger threshold. The trigger occurs when the deposited energy in the first detector is higher than 220 keV [1]. However, as it can be seen in figure 3.7, the mean deposited energy in this detector is much lower than the trigger, with a maximum at 150 keV. Particles with energies below 220 keV can still trigger events due to fluctuations in the trigger threshold and input signal. Nevertheless the sensitivity of BERM to electrons is highly reduced by the fact that only a small fraction of the particle triggers the events. The electron channels are also affected by the proximity between the BERM threshold and thresholds that distinguish between electrons and protons. That is the reason that some proton channels are more sensitive to electron channels than some electron channels. (see figure 3.9)

The electron channels (figure 3.7) present very different characteristics compared to proton channels (figure 3.10). E2 is always the channels with the highest electron geometric factor, independently of the primary energy excluding only a small range at low energies. From E2 to E5 the maximum amplitude decreases, being less likely for an electron to be attributed to higher electron channels. Channels E1 is the only exception. This behaviour is related with the fact that E1 and E2 are connected to the same detector, but different parts of the spectrum. Electron channel E2 receives events with energy deposited between 128-349 ADC (153-417 keV), and channel E1 receives events with energy deposited lower than 127 ADC (152 keV, BERM trigger threshold is 180 ADC or 215 keV). Therefore, channels E1 only receives events that passes the trigger threshold, but have deposit less than 127 ADC. This is possible due to the dispersion associated to the trigger threshold, but substantially lowers the probability that an event is attributed to this channels.

From the shape of the response functions, channels are either differential and integral. The difference lays on the range of energies that a channel is sensitive to. A differential one has a finite range of initial energies with a high geometric factor and is not very sensitive to other electron energies. An integral channel is sensitive to electrons above a given initial electron energy. Even so all electron channels response function have similar shapes, channels E1 and E2 were considered differential channels, because of the decrease of the geometric factor after the initial peak. The other channels, E3-E5 were considered integral channels.

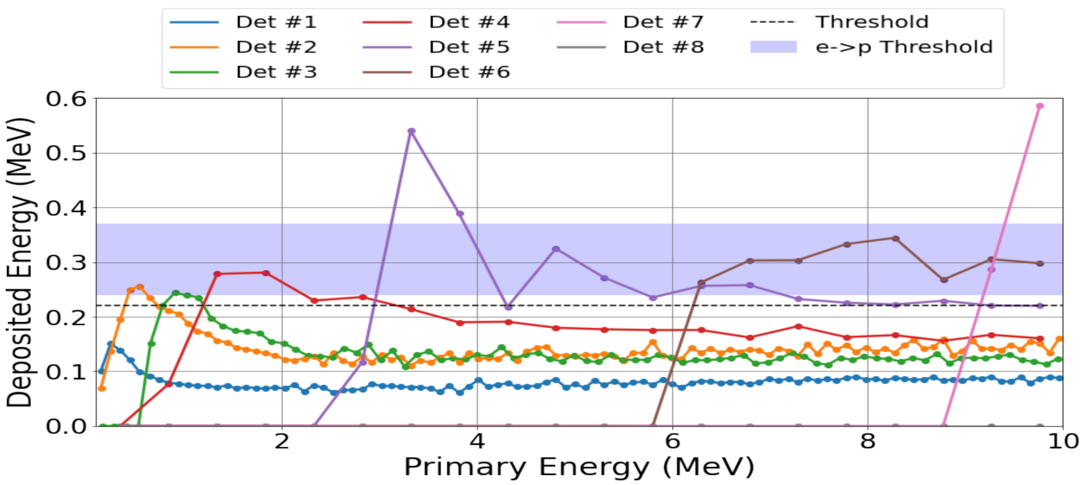

Figure 3.7: Mean deposited energy by electrons, as a function of the primary energy of the particle. The blue area represents the interval of energy thresholds that separates electron channels from proton channels. (Adapted from [10])

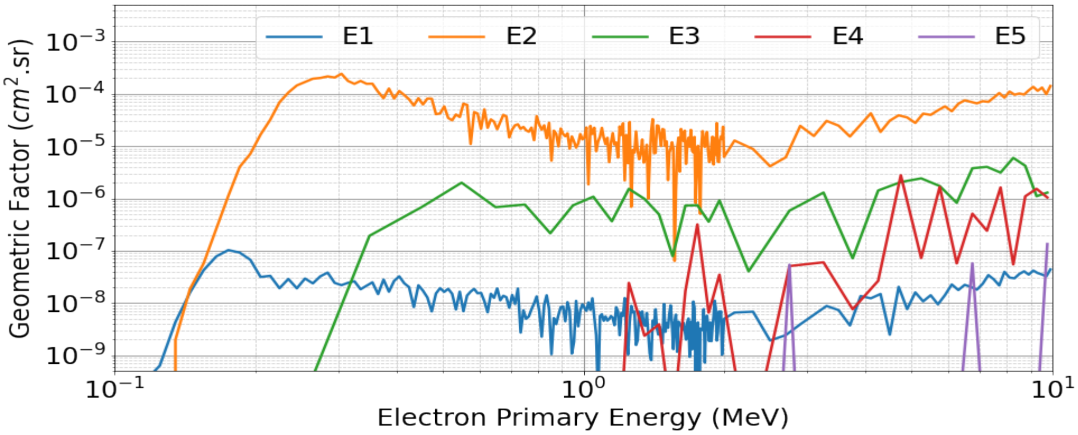

Figure 3.8: Electron channels response function. (Adapted from [10])

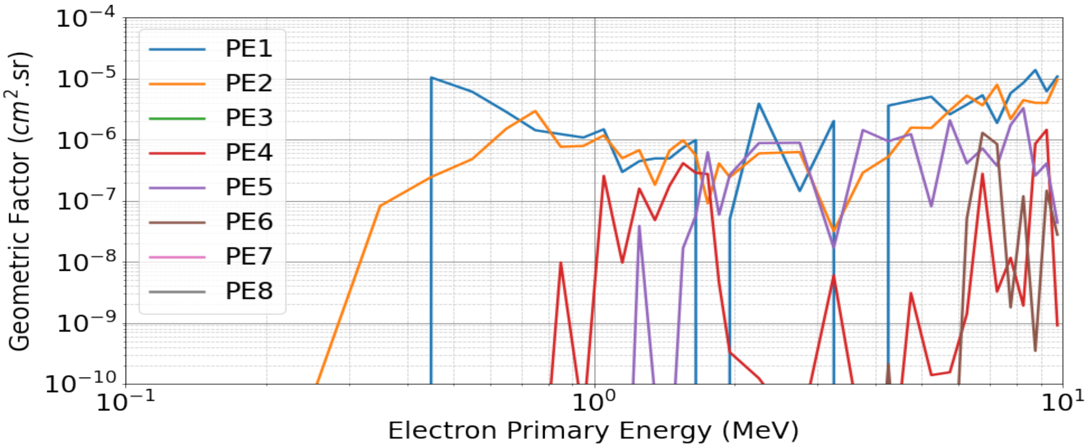

Figure 3.9: Proton channels sensitivity to electrons. (Adapted from [10])

3.5.2 Proton Response Function

The same method used for electrons was applied for protons. Figures 3.10, 3.11 and 3.12 show the mean energy deposited by protons in the detectors as function of the primary energy, proton channels response functions, and electron and heavy ion channel sensitivity to protons, respectively.

Figure 3.10 was obtained in the same conditions as figure 3.7, simulating the deposited energy of protons in all detectors. The thresholds for distinguishing between different types of particles, as well as the BERM energy threshold are also shown. The main characteristics of these functions are the same as for electrons. It is also possible to see the shift of the peak towards higher energies as the detector is deeper in the stack. The geometric factor increases for proton energies close to 100 MeV, something that was not observed for electrons. This occurs because at this energy protons start to pass through

the colimator material. As a consequence, when entering the stack, protons have less energy than they would have without crossing the colimator. Their behaviour is therefore similar to lower energy particles entering the collimater aperture.
As it can be seen in figure 3.11, channels P1-5 are differential while channels P6-8 are integral. EP1 and EP2 are also differential even though their geometric factor is much lower due a combination of lower deposited energy and low threshold (see figure 3.12). The main characteristics of the proton response functions are:

- Differential channels, have high geometric factor when the curves of deposited energy associated to its detector is above all other detectors. This is in agreement with the particle identification algorithm, presented in section 3.3.3, since the event is attributed to the channels connected with the detector with the higher energy deposited.
- Proton channel P3 is sensitive to less energetic protons than P2. This swap occurs because these two channels are assigned to the same detector, #2. On BERM's algorithm both channels use the energy deposited in the first BERM detector (#1, the detector immediately before the one with the maximum deposited energy). However according to the Bethe-Bloch function for protons, in this energy range, protons with higher primary energies deposited less energy, resulting in more energetic protons being assigned to P2 rather them P3.
- Channels P3 also have a distinct characteristic from the others. Proton deposited energy is between electrons and heavy ions. This means that proton channels can be contaminated by these two particles and that protons can contaminate electron and heavy ion channels. P2 and P3, being connected to the same detector, P2 only have electron contamination and P3 only have heavy ion contamination. The main consequence is that P3 in practice should be the cleanest channels, without contamination, because BERM does not detect much heavy ions during this mission.
- Channels P1 and P2 show a peak between 100 MeV and 200 MeV. These channels are very sensitive to energetic protons because above 100 MeV the collimator starts to let the particles pass through, and only the first detector needs to have a signal to add events to these channels.
- It can be seen in each proton channel response function, drops in geometric factor at different energies. The most notable is the one that appears in P3 around 8 MeV, but there are 7 in total, marked with dashed vertical lines in figure 3.11. This drops corresponds to protons with primary energies that are assigned to heavy ions channels. Therefore, for each drop in a proton channel, there is a matching peak in HIP channel, with corresponding amplitudes. This contamination occurs in channels that are connected with the same detectors: (P1,P2,P3)-HI1; (P4,P5)-HI2; P6-HI3; P7-HI4; P8-HI5. In figure 3.10 is possible to see (also marked with dashed vertical lines) that this features occurs at the peaks of the deposited energy in each detector. The higher the peak in the figure 3.10, the higher the drop in figure 3.11. The same behaviour is not seen in EP

channels due to the fact that this channels only have high amplitudes outside the box part of proton channels.

- It is important to notice that for high energies the mean deposited energy in the detectors is close to the trigger threshold that separates electrons and protons, increasing the contamination of the electron channels. In the first detector, this happens between ~1-2 MeV, causing a peak in EP1 and EP2.

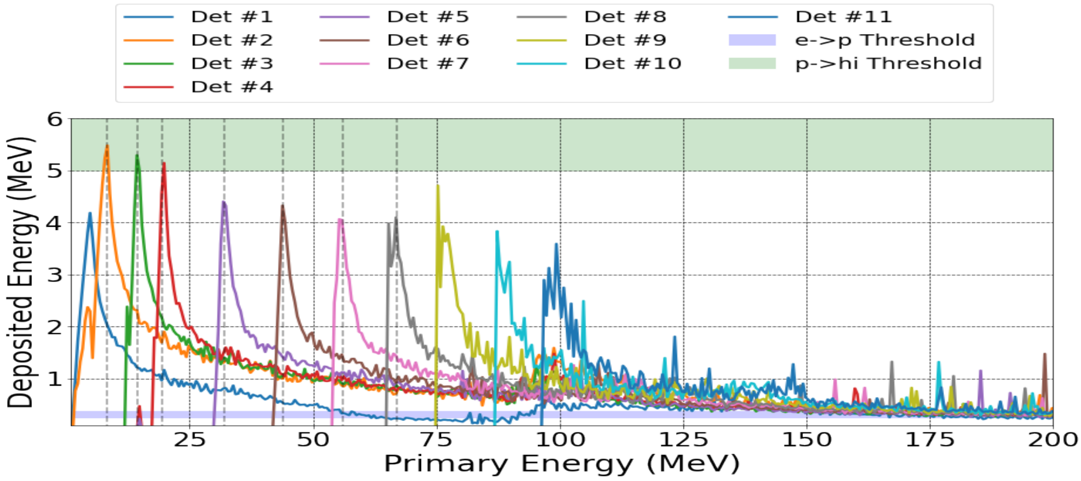

Figure 3.10: Mean deposited energy by protons, as a function of the primary energy of the particle. (Adapted from [10])

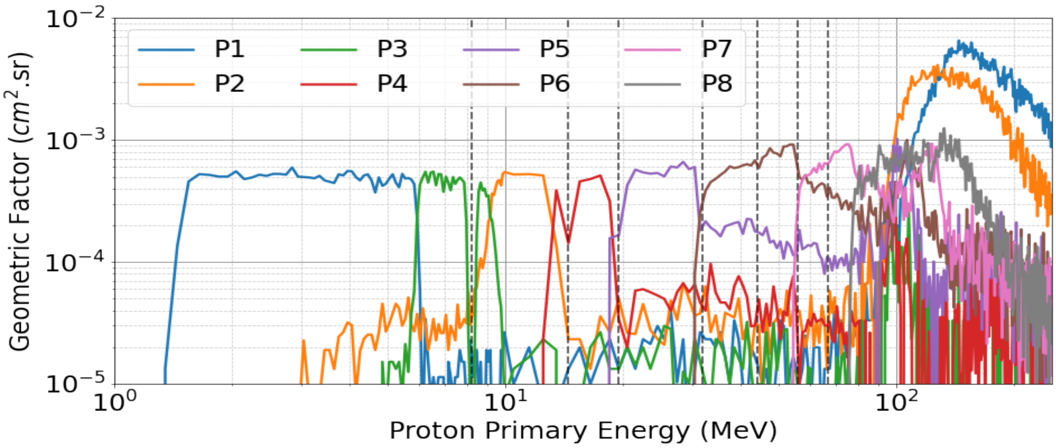

Figure 3.11: Protons channels response function. (Adapted from [10])

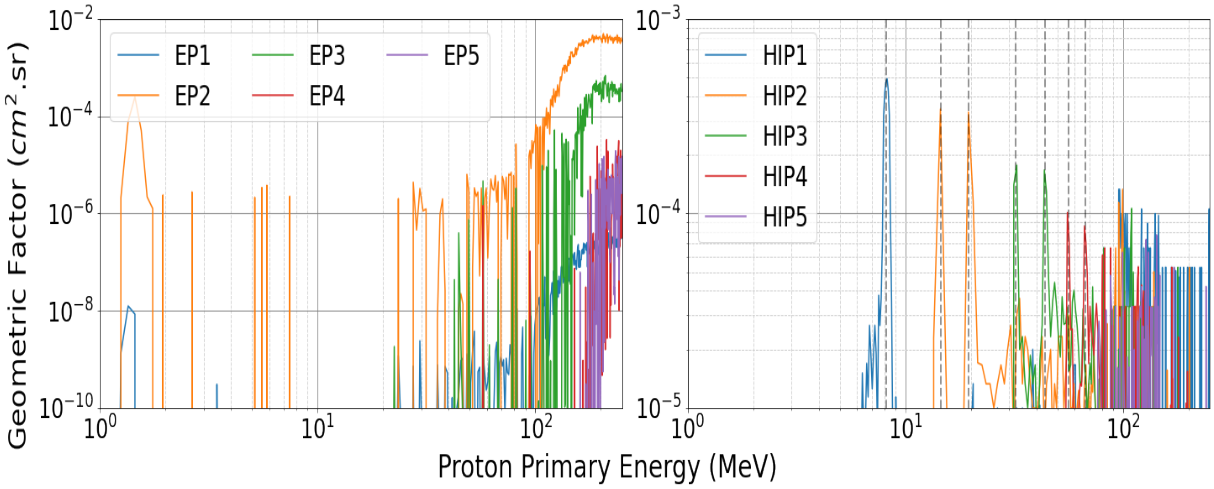

Figure 3.12: Electron channels sensitivity to protons (left). Heavy ion channels sensitivity to protons (right). (Adapted from [10])

3.5.3 Bow-Tie Method

BERM electron and proton channels were analysed in [10] using the bow-tie method and the effective geometric factor (G$_{eff}$) and an effective energy (E$_{eff}$) were obtained for each channel. This analysis has the purpose of computing a particle flux, ϕ(E), from the count rates of a channel, inverting the eq. 3.6. ϕ(E) can be computed with equations 3.7 and 3.8, depending on whether the channel is differential or integral, respectively. This method considers an energy spectrum described by a power law $\phi(E) \sim E^{-\gamma}$, with a spectral index γ [13].

With this method, E$_{eff}$ has different meanings in differential and integral channels. For integral channels, E_{eff} represents the minimum energy of the particles considered for the flux. For differential channels, E_{eff} represents the mean energy of the channel. Due to this difference E_{eff} should only be compared with channels of the same type.

$$R_{ch} = \int_0^{\infty} \phi(E) F_R(E)\, dE \tag{3.6}$$

$$\phi(E_{eff}) = \frac{R}{G_{eff}} \quad [s^{-1} \cdot sr^{-1} \cdot cm^{-1} \cdot MeV^{-1}] \qquad --> \qquad \text{Differential Channel} \tag{3.7}$$

$$\phi(E > E_{eff}) = \frac{R}{G_{eff}} \quad [s^{-1} \cdot sr^{-1} \cdot cm^{-1}] \qquad --> \qquad \text{Integral Channel} \tag{3.8}$$

The results of the bow-tie method obtained in [10] are presented in tables 3.7 and 3.8. Table 3.7 describes BERM electron and proton channels sensitivity to electron and protons (EX and PX), respectively. Table 3.8 describes BERM electron and proton channels sensitivity to protons and electrons (EPX and PEX), respectively. From this analysis, three results must be highlighted:

- Electron channels E1 has a geometric factor 3 order of magnitude lower than channels E2. As it will be demonstrated in this thesis, this result consists in a bad reconstruction of channels E1. This shortcoming is the main motivation for this thesis.
- The result obtained with proton channels P2 and P3 are in agreement with figure 3.11. The effective energy of channels P3 is lower than channels P2.
- The high error obtained in proton channels P1 and P2 is a consequence of the high sensitivity of these channels to high energetic protons.

Channel	Channel Name	Type	E_{eff}(MeV)	GdE($cm^2 \cdot sr \cdot MeV$)	$G_I(cm^2 \cdot sr)$	σ_{min}	δ_G^-		δ_G^+	
1	E1	Dif	0.21	$1.02{\cdot}10^{-8}$	-	0.033	$-3.27{\cdot}10^{-10}$	-3%	$7.46{\cdot}10^{-10}$	7%
2	E2	Dif	0.32	$4.36{\cdot}10^{-5}$	-	0.029	$-1.28{\cdot}10^{-6}$	-3%	$2.67{\cdot}10^{-6}$	6%
3	E3	Int	0.35	-	$8.53{\cdot}10^{-7}$	0.023	$-1.00{\cdot}10^{-8}$	-1%	$1.22{\cdot}10^{-8}$	1%
4	E4	Int	2.18	-	$3.30{\cdot}10^{-7}$	0.023	$-2.49{\cdot}10^{-8}$	-8%	$1.43{\cdot}10^{-8}$	4%
5	E5	Int	2.63	-	$7.87{\cdot}10^{-9}$	0.003	$-7.18{\cdot}10^{-10}$	-9%	$4.13{\cdot}10^{-10}$	5%
6	P1	Dif	2.73	$2.23{\cdot}10^{-3}$	-	0.086	$-1.97{\cdot}10^{-4}$	-9%	$3.62{\cdot}10^{-4}$	16%
7	P2	Dif	13.46	$8.25{\cdot}10^{-3}$	-	0.189	$-1.62{\cdot}10^{-3}$	-20%	$3.01{\cdot}10^{-3}$	37%
8	P3	Dif	7.36	$1.47{\cdot}10^{-3}$	-	0.013	$-2.11{\cdot}10^{-5}$	-1%	$3.72{\cdot}10^{-5}$	3%
9	P4	Dif	17.65	$3.62{\cdot}10^{-3}$	-	0.021	$-8.35{\cdot}10^{-5}$	-2%	$1.40{\cdot}10^{-4}$	4%
10	P5	Dif	29.22	$1.34{\cdot}10^{-2}$	-	0.029	$-4.17{\cdot}10^{-4}$	-3%	$7.13{\cdot}10^{-4}$	5%
11	P6	Int	27.17	-	$3.91{\cdot}10^{-4}$	0.019	$-1.38{\cdot}10^{-5}$	-4%	$8.44{\cdot}10^{-6}$	2%
12	P7	Int	47.23	-	$3.63{\cdot}10^{-4}$	0.015	$-1.00{\cdot}10^{-5}$	-3%	$6.03{\cdot}10^{-6}$	2%
13	P8	Int	70.6	-	$4.63{\cdot}10^{-4}$	0.009	$-8.11{\cdot}10^{-6}$	-2%	$4.82{\cdot}10^{-6}$	1%

Table 3.7: Characteristic energies and geometric factors of BERM channels. [10]

Channel	Channel Name	Type	E_{eff}(MeV)	$G_I(cm^2 \cdot sr)$	σ_{min}	δ_G^-		δ_G^+	
1	EP1	Dif	1.38	$2.18{\cdot}10^{-9}$	0.001	$-4.60{\cdot}10^{-12}$	-0.2%	$7.44{\cdot}10^{-12}$	0.3%
2	EP2	Dif	1.44	$3.87{\cdot}10^{-5}$	0.001	$-4.18{\cdot}10^{-8}$	-0.1%	$1.02{\cdot}10^{-7}$	0.3%
3	EP3	Dif	223.2	$5.53{\cdot}10^{-2}$	0.010	$-5.98{\cdot}10^{-4}$	-1%	$1.05{\cdot}10^{-3}$	2%
4	EP4	Dif	228.72	$8.48{\cdot}10^{-4}$	0.024	$-2.22{\cdot}10^{-5}$	-0.04%	$3.75{\cdot}10^{-5}$	0.1%
5	EP5	Dif	293.19	$2.89{\cdot}10^{-3}$	0.004	$-1.41{\cdot}10^{-5}$	-0.5%	$2.44{\cdot}10^{-5}$	1%
6	PE1	Int	0.29	$3.06{\cdot}10^{-6}$	0.018	$-9.74{\cdot}10^{-8}$	-3%	$6.72{\cdot}10^{-8}$	2%
7	PE2	Int	0.47	$1.16{\cdot}10^{-6}$	0.031	$-3.91{\cdot}10^{-8}$	-3%	$7.19{\cdot}10^{-8}$	6%
10	PE5	Int	1.91	$8.70{\cdot}10^{-7}$	0.006	$-5.86{\cdot}10^{-9}$	-1%	$9.72{\cdot}10^{-9}$	1%

Table 3.8: Characteristic energies and geometric factors of BERM electron channels measuring protons (EPX) and proton channels measuring electron (PEX). [10]

3.6 BERM Flyby Data Comparison

To validate BepiColombo Environment Radiation Monitor (BERM) response functions data obtained with BERM during the BepiColombo flyby are compared in this work to SIXS-P [7] observations during the same period, and to AE8/AP8 and AE9/AP9 modeled data of the flyby [30, 31]. Bepicolombo Earth flyby geometry is presented in figure 3.13.

Both analysis can contribute differently to validate BERM's data. These models are static and show only average fluxes - AE9/AP9 can provide fluxes within confidence intervals but is still under construction. For example, the outer belt, swells and shrinks over time, changing the particle flux spacial dependence.

Comparing the data with other instruments with overlapping capabilities aboard the same spacecraft, allows to overcome this drawback. However, other instruments require also validation and suffer from systematic uncertainties that need to be taken into account.
Figure 3.14 shows the comparison between BERM's data and models AE8/AP8 and AE9/AP9, for E1-E3 and P1, during the Earth flyby. AE8/AP8 and AE9/AP9 are integrated with channels geometric factor in order to obtained the expected count rate of each channels.

$$CR_{A8/9} = \int_{E_{min}}^{E_{max}} GF_E(Ch, E) * AE8/9(E) + GF_P(Ch, E) * AP8/9(E)\, dE \tag{3.9}$$

Ch is the channels that is being analysed, E the energy and E_{min} and E_{max} the boundaries of the model. GF$_E$ (GF$_P$) is the response function for electron (protons) for that channel. For protons (electron) channels GF$_E$ (GF$_P$) corresponds to contamination from electrons (protons). The results is the count rate of each channel. E_{min} was set to a lower value than any response functions lower bound. E_{max} was equal to the limit energy for that type of channels (10 MeV for electrons and 100MeV for protons).
In figure 3.14 it can be seen both the inner and the outer belt. The first peak of particles is within the outer belt. The two following peaks correspond to the inner belt (not see in E3), and the last peak is again the crossing of the outer belt. This is a consequence of the BepiColombo flyby geometry. Two peaks are observed in the inner belt due to the spacecraft rotation changing BERM's pointing direction. The models used consider omni-directional particle flux hence this cannot be fully reproduced. Between electron bins and protons bins, it is also possible to see the difference in sensitivity to different types of particles. Electrons bins have more counts in the outer belt, composed mainly by electrons. The protons bins have more counts in the inner belt, with a higher composition of protons.
E2 and P1 are in close agreement with the A8 and A9. There is only a slightly difference in P1, especially in the inner belt, due to the lack of the second peak in the models. However, the first and third electron bins have a significant difference between flight data and A8/A9 estimations. This difference was around 3 orders of magnitude for E1 and one order for E3, an indication that BERM's response functions were not accurate. Figure 3.15, comparing BERM's and SIXS-P Earth flyby data, draws the same conclusions.
In figure 3.15, BERM and SIXS-P fluxes were computed with the following expressions:

$$F = \frac{N}{\tau} \frac{1}{G\delta E} \frac{1000}{1000 - \tau_D} \tag{3.10}$$

Where F is the flux, N is the particle count, GδE is the differential geometric factor of a channel obtained by the Van Allen Bow-tie analysis, τ is the integration time, and τ_D is the average dead time in milliseconds. BERM dead time was considered zero for all channels.
Figure 3.15 shows the comparison between BERM and SIXS-P channels with energies close to BERM's channels. As it can be seen, BERM E1 has has a larger flux than SIXS-P E4, with similar effective en-

ergy. This difference is not observed in BERM P1 and SIXS-P P4. In these channels, only small differences are observed which can be attributed to electron contamination and pointing direction. Correctly modeling E1 and E3 is the main objective of this thesis.

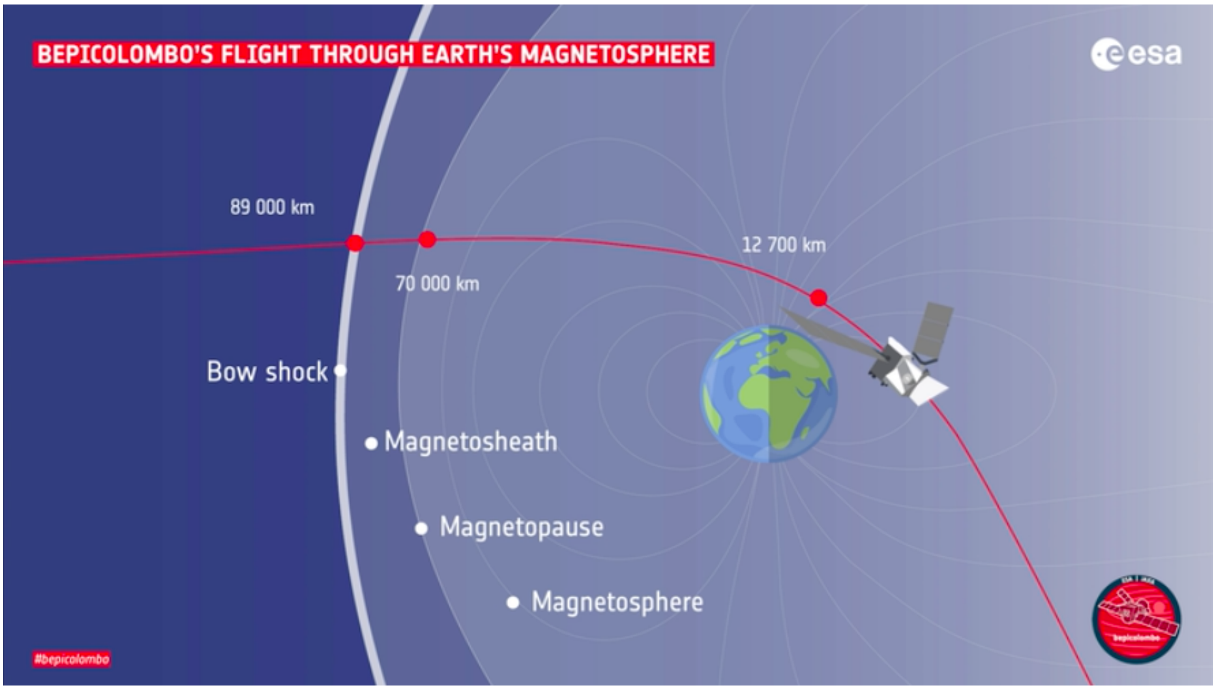

Figure 3.13: Geometry of Bepicolombo Earth flyby

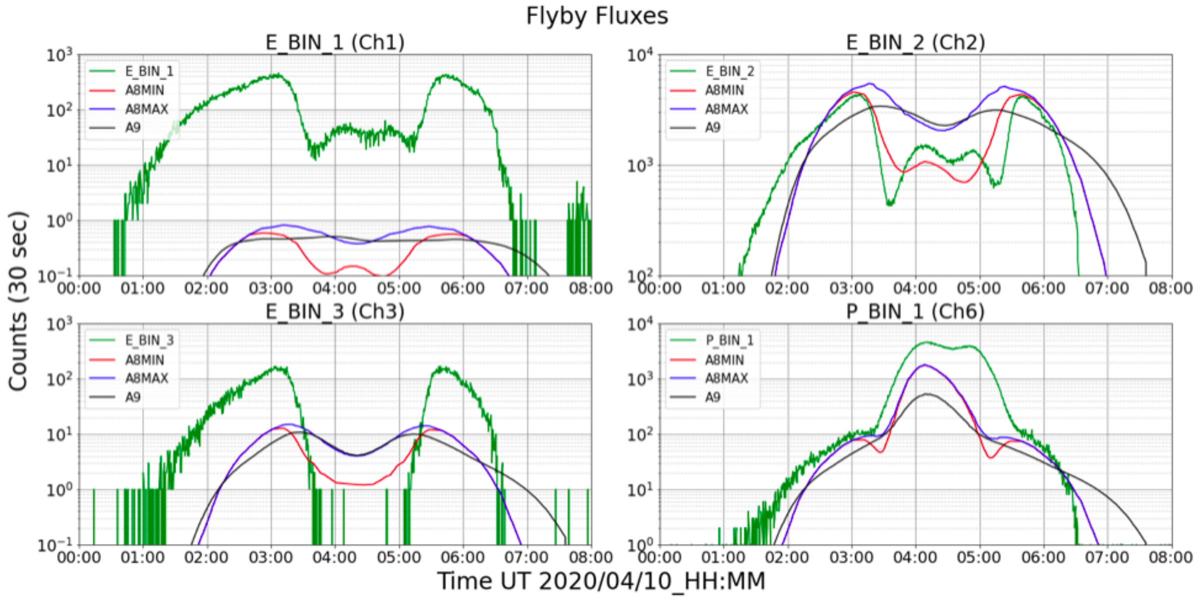

Figure 3.14: Comparison between BERM's data and models A8 and A9, for E1, E2, E3 and P1, during the Earth flyby.

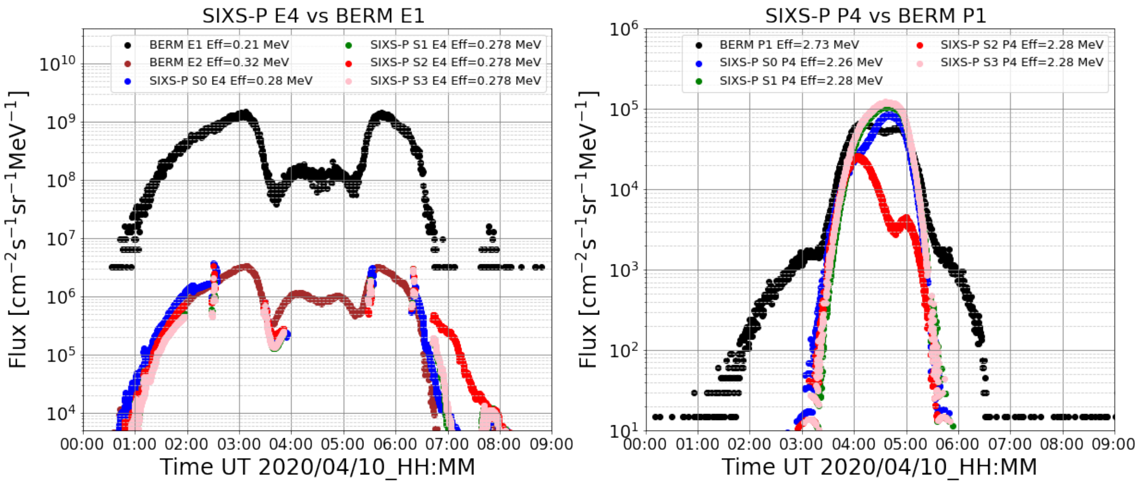

Figure 3.15: Comparison between BERM's and SIXS-P's data during the Earth flyby.

4

BERM Characterisation with Radioactive Sources

Contents

To study and characterise the shortcomings of BepiColombo Environment Radiation Monitor (BERM)'s flux reconstruction of the Earth flyby, a battery of tests were performed with the BERM Engineering Qualification Model (EQM), available on-ground. Two radioactive beta emitters, 137-Cs and 90-Sr, were used. These sources emit electrons with energies below 2.289 keV which allows to study the first detectors (the decay chain of both sources are shown in figure 4.1). The main objectives were to calibrate the trigger threshold, which was not done during the 2014 calibration campaign of BERM, and to model and study the effect of the cross-talk identified in [1]. These tests were performed in spectral mode to obtain the energy deposited in all detectors for each event.

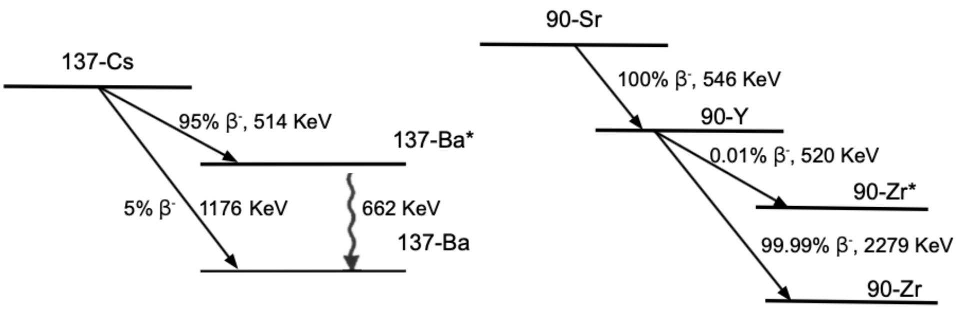

Figure 4.1: Emission diagram of 137-Cs and 90-Sr.

4.1 Threshold Analysis

The trigger threshold was the first parameter analysed. If the threshold used to produce BERM response functions is higher than the operational value, the flux reconstructed will be lower than the real value which could explain the results obtained for E1 and E3. For this analysis, a spectrum of the deposited energy in the first detector, for different threshold values was acquired. The threshold is a parameter that can be changed in BERM, in a nominal scale of -15 to 15. The value used in BERM, is Th=0, and the goal of this analysis is to obtain a calibration curve for this parameter, that relates the nominal scale with an energy scale to extract the value of the threshold, in units of energy, for Th=0.

Figures 4.2 and 4.3, show the spectrum of the deposited energy in the first detector obtained using 137-Cs and 90-Sr, respectively. In figures 4.2 and 4.3 the energy was converted to MeV, inverting the Analogue-to-Digital Converter (ADC) value, removing the noise pedestal and applying the conversion factor from ADC to MeV (presented in table 3.2). To obtain the threshold energy value, data obtained for each nominal threshold value were fitted to an exponential function multiplied by a Gaussian cumulative distribution function (CDF) (eq. 4.3). The Gaussian (CDF) (eq. 4.1) fits the threshold behaviour, creating a cut-off energy with a dispersion as suggested in [1]. The exponential recreates the energy deposition spectrum (eq. 4.2).

$$\text{Gauss}_{\text{CDF}}(x, \mu, \sigma) = \frac{1}{2}\left(1 + Erf\left(\frac{x-\mu}{\sqrt{2}\sigma}\right)\right) \tag{4.1}$$

$$\text{Spectrum(x,C}_1\text{, C}_2\text{, C}_3) = C_1 * exp^{-C_2*(x-C_3)} \tag{4.2}$$

$$\text{f} = \text{Gauss}_{\text{CDF}}(x, \mu, \sigma) * \text{Spectrum(x,C}_1\text{, C}_2\text{, C}_3) \tag{4.3}$$

To fit the data it could also be used a simulation of the spectrum of the deposited energy instead of the exponential. However, as it will be analysed in subsection 4.3, the simulation does not fully reproduce the acquired spectrum. The cross-talk between detectors changes the energy spectrum, and by consequence, the exponential fits better the data then the simulation.

Figure 4.4 presents the threshold calibration curve. This curve (y=ax+b) presents a slope a=-0.0033 MeV and a horizontal shift b=0.205 MeV. A trigger threshold of 0.205 MeV is thus found for th=0. This result is similar to the value obtained in [1], especially taking in consideration that it was obtained for the EQM, a different instrument, that despite being a replica of BERM, should have (small) electronic deviations. Even so, the new threshold value was used to produce new response functions, and the result was a small change towards the BERM's data. AE8/AP8 and AE9/AP9 models are now in closer agreement with the data for Bins E1 and E3, however this small change is not enough to explain the big difference between data and the models in these channels (see figure 4.5).

The threshold analysis yields a smaller value than the 220 keV value from the BERM ground calibration. However the difference is not enough to explain the issue found in the electron channels for the Earth flyby. This analysis also shows that, in principle, the threshold could be lowered to 160 keV which would make BERM more sensitivity to electrons.

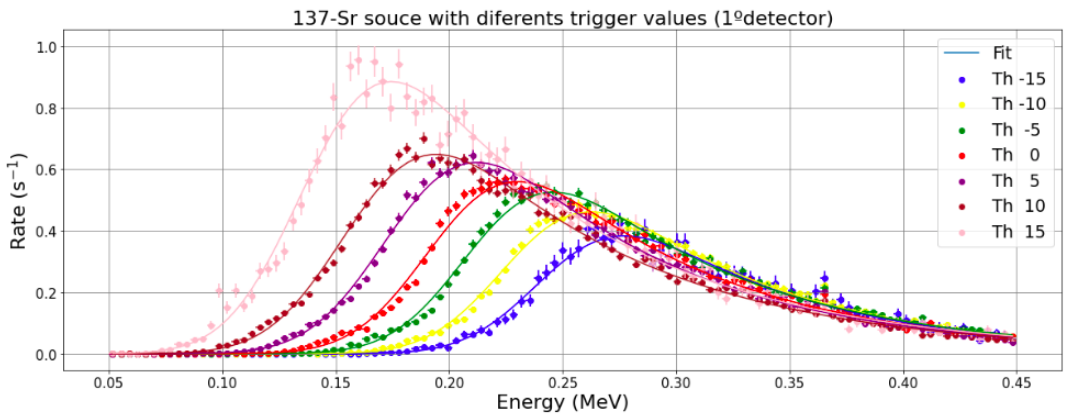

Figure 4.2: Comparison of the energy deposited spectrum with 137-Cs with different threshold values.

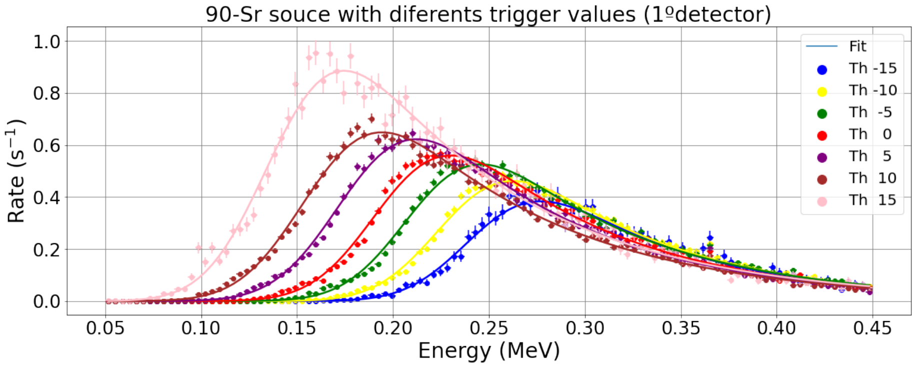

Figure 4.3: Comparison of the energy deposited spectrum with 90-Sr with different threshold values.

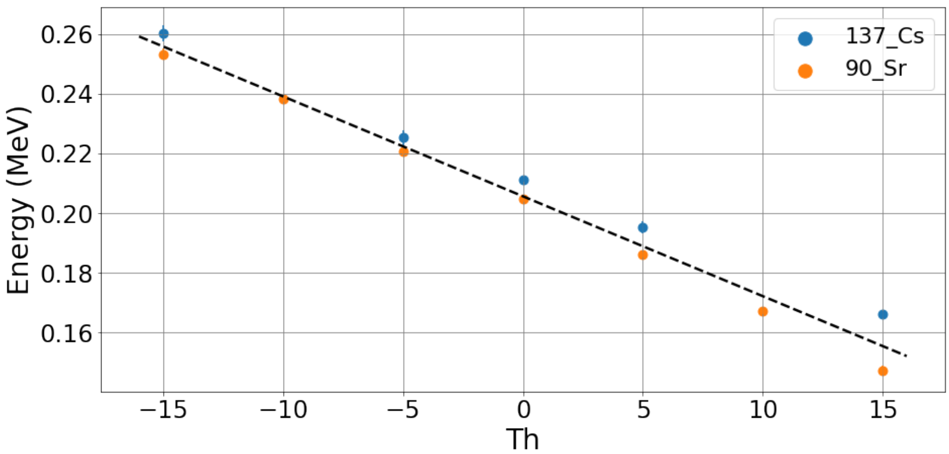

Figure 4.4: Threshold calibration curve. Threshold calibration curve. The linear fit (y=ax+b) parameters are b=0.204 and b=0.0033.

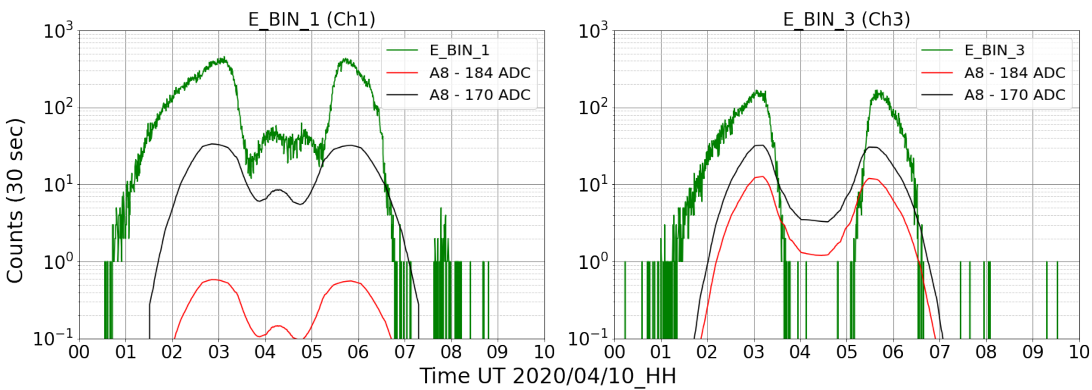

Figure 4.5: Comparison between BERM EQM E1 and E3 channels simulation of Earth flyby, using the trigger threshold set at 220 MeV and 204 MeV.

4.2 Electrical Noise

All detectors have electronic noise, producing signals even without particles interacting with them. This signal has the shape of a Gaussian, where the mean value corresponds to the pedestal of each detector. In the signal processing chain, this value is subtracted to the output of each detector. However, detectors with electronic noise with larger standard deviation can have significant signals even after the subtraction of the pedestal. This can lead to events being attributed to the wrong channel if the signal produced by a particle is lower than the noise in one of this detectors. It is then important to study the effect of noise in the response functions.

Table 4.1 present the noise parameters of all detectors. The pedestal does not show any correlation with any detector characteristic. However the standard deviation increases with detector area. The exception is detector 11 that has a standard deviation lower than the detector 7.

As a consequence of the large dispersion of the electrical noise in the final detectors of the stack, which have larger areas, channels P8 (or channel 13 that corresponds to proton eighth channel, P8, where the correspondence between BERM 20 channels and the specific electron, proton and ion channels was described in table 3.4)) is unstable and sensitive to the temperature. This channel is the first connected to detectors 9, 10 and 11, so any event that deposits less energy (in ID_{max}) than the noise on one of these detectors, can be attributed to channels 13. Additionally temperature variations inside BERM, changes noise values and consequently the behaviour of this channel.

Figure 4.6 shows the background of all detectors obtained experimentally. Each line corresponds to a measurement. Figure 4.7 shows the background obtained via Monte Carlo simulations using a Gaussian distribution (see table 4.1) for each detector and assuming no correlation between the detectors. Has it can be seen, the pedestals of the detectors are well simulated, however experimental data presents a correlation between different detectors that was not being taken in consideration in the simulation. In Appendix A a plot with the deposited energy obtained with a 90-Sr source, for each combination of consecutive BERM detectors is shown. For the last detectors, where there is only noise, it is possible to see the correlation between the noise of consecutive detectors. Figure 4.8 presents the result of applying BERM reconstruction algorithm to data obtained with 90-Sr, adding correlated and uncorrelated noise. It also presents the Geant4 simulation of BERM response to 90-Sr, without taking in consideration noise correlation. During this work, the noise correlations it were not modeled, so to add this effect to BERM EQM 90-Sr data, experimental values of noise correlation was added to each event, as presented in figure 4.6. Because only electron and gammas are emitted, every event associated to channels 6 to 18 is contamination. Noise correlation between the detectors presents a significant change in channel 13, as expected. Events assigned to this channel were taken from all electron channels, not impacting significantly any of those channels. However the simulation output of channels 13 is now much closer to the one obtained with data. This means that the noise correlation needs to be included in the analysis since it can mimic particle signatures, although it cannot explain the issues found in electron channels E1 and E3.

The noise correlation presented in this section can indicate that the source of the noise is in the ASIC rather than the detectors.

Detector #	1	2	3	4	5	6	7	8	9	10	11
Noise Pedestal (ADC)	1489	1559	1587	1460	1389	1452	1541	1387	1283	1434	1447
Std (ADC)	12.25	14.18	14.43	20.19	31.10	63.56	83.27	89.52	135.45	138.81	81.40

Table 4.1: Noise parameters for all BERM detectors.

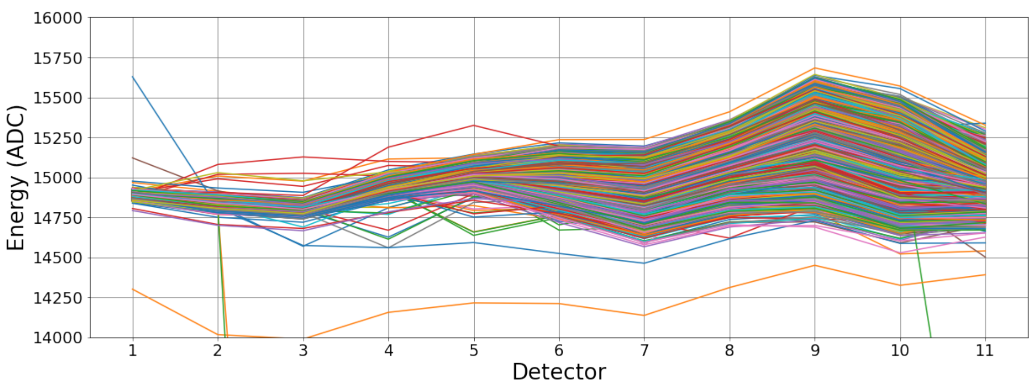

Figure 4.6: Background signal of all BERM EQM detectors. Each line corresponds to a measurement.

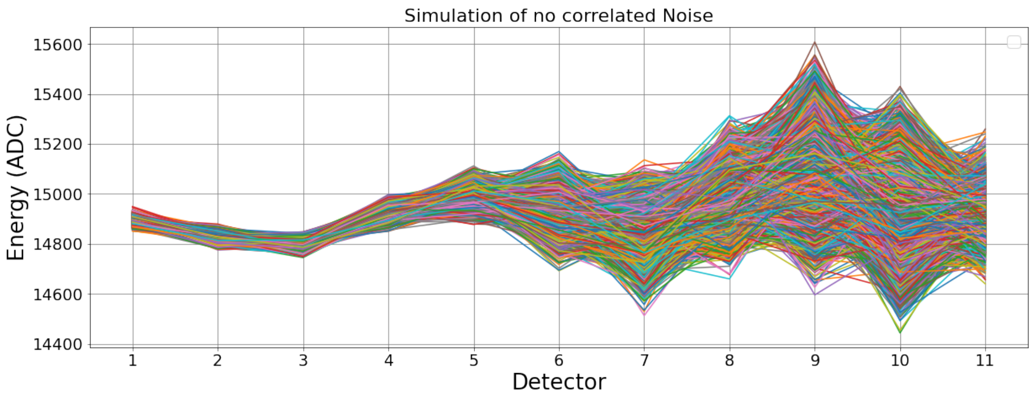

Figure 4.7: Background obtained via Monte Carlo simulations using a Gaussian distribution of the background in each detector and assuming no correlation between the detectors. Each line corresponds to a measurement.

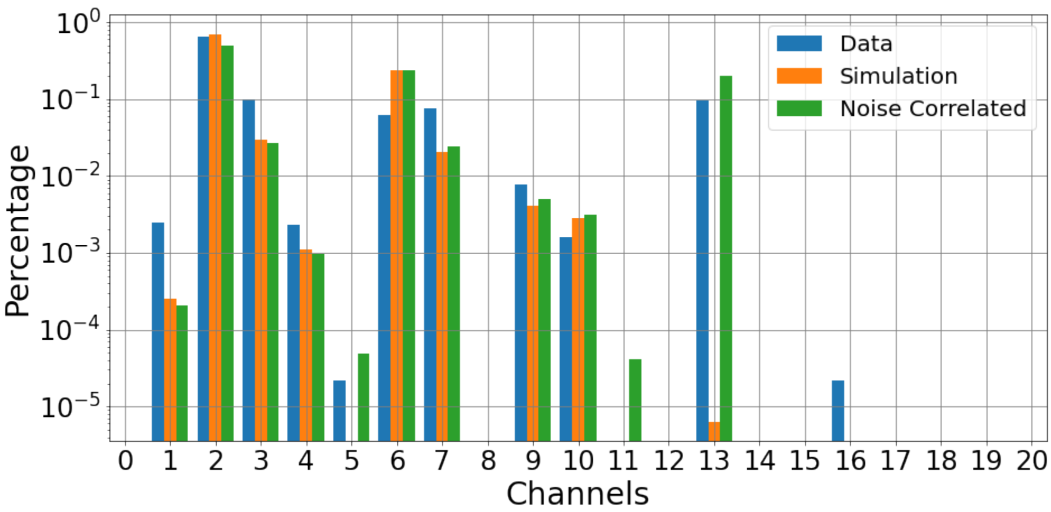

Figure 4.8: Blue: 90-Sr data; Orange: 90-Sr simulation without noise correlation between BERM EQM detectors; Green: 90-Sr simulation with noise correlation between BERM EQM detectors.

4.3 Cross-Talk Analysis

The cross-talk between BERM detectors was also analysed. This effect is characterised by undesired charge sharing between two independent electrical circuits, due to undesired capacitive, inductive, or conductive coupling between both circuits. To analyse this characteristic of the instrument, data obtained with the radioactive sources 90-Sr and 137-Cs was used and Geant4 simulations were performed. Figure 4.9 (middle) shows the correlation between the energy deposited in the first and second detectors. The cross-talk is the linear component found in data, marked in figure 4.9 (middle). In the simulations, (see figure 4.9 left) there is a high number of events on top of the horizontal axis, corresponding to have only deposited energy in the first detector. However, no such events exist in the Sr-90 source experimental data. Instead, a linear component between detectors 1 and 2 compatible with events that have lost energy in the first detector and gained energy in the second. This component is interpreted in this work as cross-talk between detectors. However, its origin is not well understood. The most likely causes are in the close by detectors current paths, or the ASIC internal design. BERM cross-talk is also asymetric between detectors. In typical cases of cross-talk the coupling between both circuits should be symmetric. In fact, there is no evidence of events losing energy from the second detector to the first. This can be seen in figure 4.8 (right) where the trigger was set to the second detector. In this case, the area of the plot cut by the trigger threshold changed, making it possible to analyse the events around the vertical axis. In this plot, it is possible to see a linear component around the vertical axis, compatible with events that have only deposited energy in the second detector, as it is seen in the simulation.

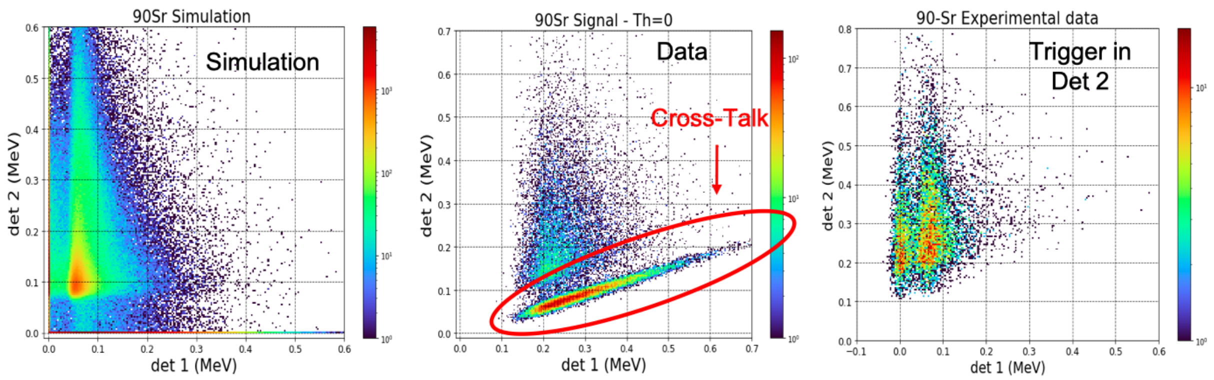

Figure 4.9: Left: Simulation of energy deposited in detectors one and two, with 90-Sr. Middle: Data obtained with EQM with 90-Sr, and trigger in the first detector (as is used in BERM). Right: Data obtained with EQM with 90-Sr, but with trigger in the second detector.

To model the cross-talk, we need to select the events subject to it, and find the percentage of energy that is crossing to the next detector. This can be obtained with the following expression:

$$P_i = \frac{E_i}{E_i + E_{i-1}} \tag{4.4}$$

Where E_i is the energy deposited in detector i, and P_i is the percentage of energy in detector i, in relation to the sum of the energies in detector i and i-1. As it can be observed in figure 4.10, applying this expression to the data obtained with BERM EQM, separates the events in two regions. At lower percentages (0.2-0.3) there is a peak that corresponds to cross-talk, followed by a more spread area of the signal. Cross-talk can be modeled with a gaussian function. In this work all detectors were individually analysed, resulting in a better description of the each detector behaviour. The result was included in BERM´s model, to produce new response functions.

To analyse this behaviour in all detectors, the original BERM calibration data using proton beams, described in [1], was used. This set of data has less statistics than the data set obtained with radioactive sources. However, the proton data were obtained with the BERM flight model instead of the EQM. Moreover, due to the range of primary energies used (protons up to 200 MeV), it is possible to analyse all detectors. Calibration data was obtained in an extensive test campaign, performed at the Paul Scherrer Institute (PSI), Switzerland, in 2014. Proton beams from the Proton Irradiation Facility (PIF) with energies ranging from 10 to 200 MeV, were used. The different energies were obtained from two initial proton beam energies, 73.5 MeV and 230 MeV using copper absorbers to decrease the beam energy. The characteristics of the proton beams can be seen in table 4.2.

Some data set were excluded from the analysis for two reasons. Either the energy is too low to reach a certain detector, or the energy flux was too high and pile-up dominated over cross-talk and signal [1]. Taking this in consideration two criteria were applied to include or exclude each data set from the analysis: It had to have sufficient events to produce an analysis. For deeper detectors in the stack, the low energetic beam are missing from the analysis, for that reason. The other criteria is that it needs to be possible to distinguish cross-talk from signal and pile-up. For higher energies and deeper detectors, this criteria exclude same of the data sets. The result of the analysis with the calibration data is presented in figure 4.11, where the percentage of cross-talk correspond to the mean values of the gaussian distributed fitted to each proton beam for each detector.

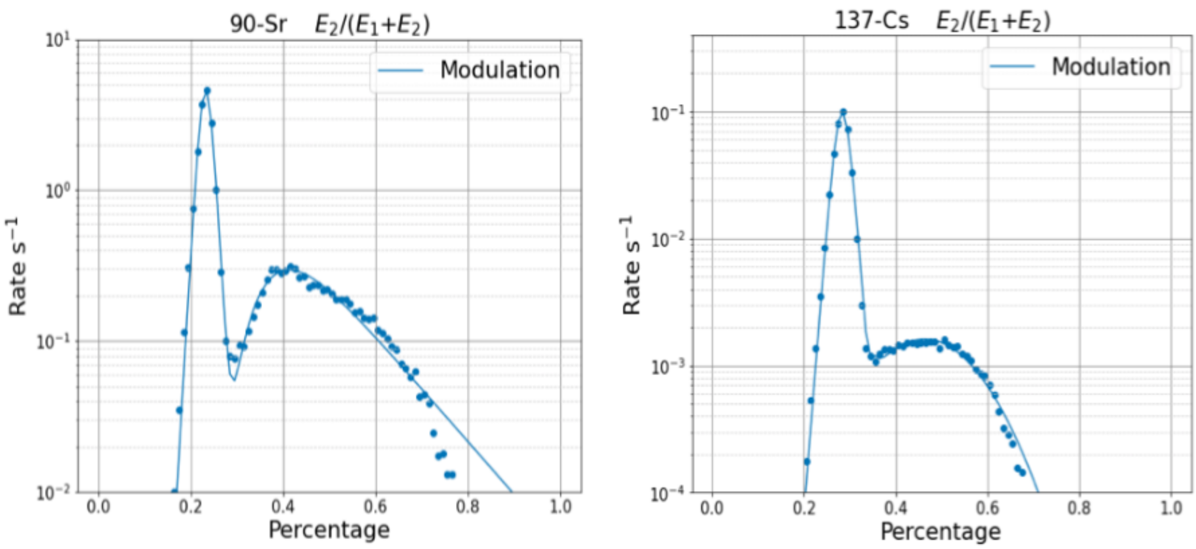

Figure 4.10: Percentage of energy deposited in second detector in relation of all energy deposited in first and second detectors.

Proton Energy (MeV)	Initial Energy (MeV)	Flux (p*cm^{-2}s^{-1})	Fluence (p/cm^2/s)	Cu thickness (g/cm^2)	Energy straggling (MeV)	Angular Dispersion (○)
200	230	5.83E+04	1.09E07	10.30	1.41	0.02
176	230	4.69E+04	1.09E07	17.92	1.84	4.05
151.2	230	3.69E+04	7.35E06	25.09	2.15	4.86
139.5	230	3.05E+04	6.29E06	28.22	2.27	5.17
115	230	2.46E+04	5.16E06	34.05	2.46	5.72
101	230	2.17E+04	4.19E06	37.09	2.55	5.99
85.4	230	1.64E+04	3.18E06	40.32	2.63	6.27
73.5	73.5	1.68E+03	3.79E05	0.00	0.00	2.00
70.8	73.5	1.53E+03	2.85E05	0.45	0.28	3.77
55.6	73.5	9.94E+02	1.82E05	2.69	0.67	7.31
40.7	73.5	6.22E+02	1.16E05	4.48	0.86	0.61
25.9	73.5	3.93E+02	7.59E04	5.82	0.97	11.05
19.2	73.5	3.10E+02	6.05E04	6.27	1.00	11.51
10	73.5	1.99E+02	3.84E04	6.72	1.03	11.94

Table 4.2: Proton energy scan beam characteristics. [1]

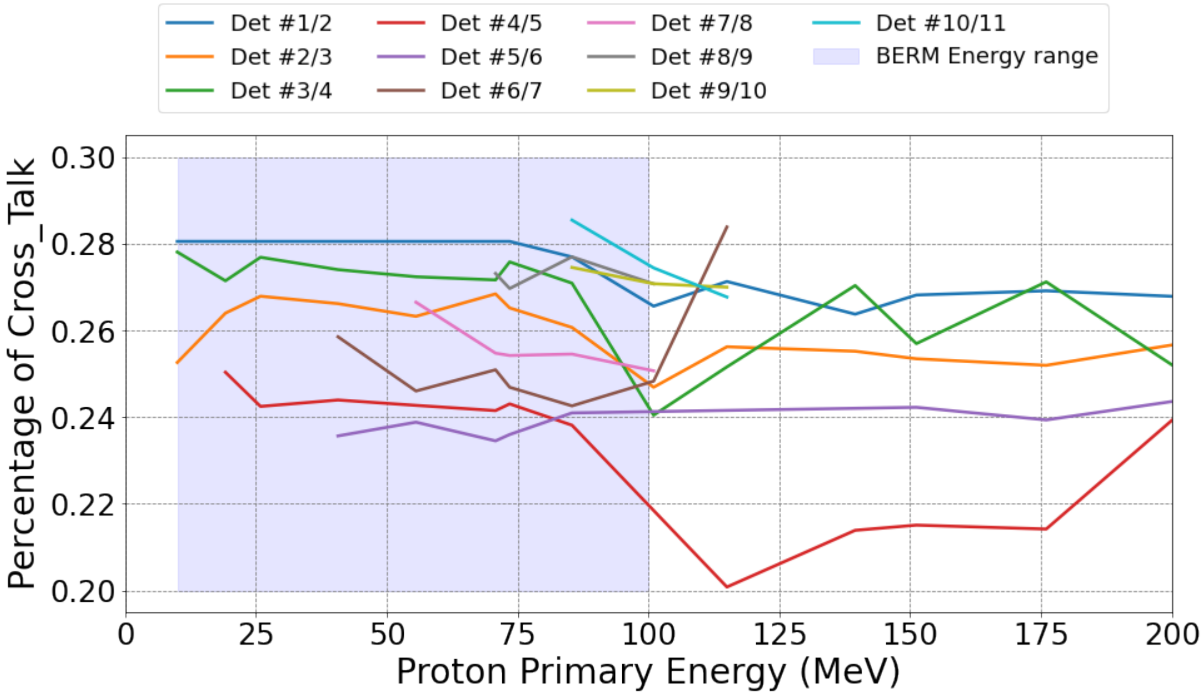

Figure 4.11: Percentage of cross-talk obtained for all detectors with proton calibration data.

4.4 Response Functions and Bow-Tie Method

With the new models of cross-talk, new response functions were computed using the methods discussed in section 3.5.3. Figures 4.12 and 4.13 present the response functions obtained with proton simulations, and figure 4.14 the response function obtained with electron simulations. Bow-tie analysis was also performed. The characteristic energies and geometric factors obtained from the bow-tie analysis are presented in tables 4.3 and 4.7 for protons channels and tables 4.6 and 4.5 for electron channels.

To obtained these response functions the trigger threshold remains at 0.220 MeV. This value yields the better results when applying the new response functions to BERM data, re-enforcing the idea that the difference between new trigger threshold obtained with BERM EQM and the value obtained in [1] with BERM, is likely due instrumental variation. The results obtained with the noise analysis were also not included in the response functions for two reasons. First, because it does not produce any significant change in the electron channels. Channel P8 is the only one with a major different result after the noise analysis. The second reason is the need of further development of this analysis. In this thesis it was possible to identify the noise behaviour and understand how influences BERM response functions, however more modulation work is needed before including this effect in the BERM response function.

Proton

Proton response functions of all channels are very similar to the ones obtained in [10] and shown in section 3.5.2. This was expected since the flux reconstruction of the Earth flyby data was already in good agreement with the A8/A9 models and the SIXS-P data. The only exception are the heavy ion channels, that don't show the features obtained before. Meaning that the contamination of the heavy ions channels by protons has decreased, and the drops in the proton channels disappeared. Contamination of the electron channels remains similar to the previous results as well.

Channels P1 and P2 keep have the highest error values, due to the high geometric factor for protons with more than 100 MeV. Protons with these energies start to pass through the collimator, increasing the geometric factor of the channels. If an event does not have such energetic protons the bow-tie analysis can be performed with the response functions below 90 MeV only. In table 4.4, the results of applying a bow-tie analysis to the response functions considering protons only up to 90 MeV show a significantly lower error. The geometric factors are also lower and similar to the geometric factor displayed in figure 4.12. The effective energy of channel P2, despite still being higher than channels P3, is also lower considering only part of the spectrum. In fact, both are very similar due to the tail of the response function of channel P2 for lower energies.

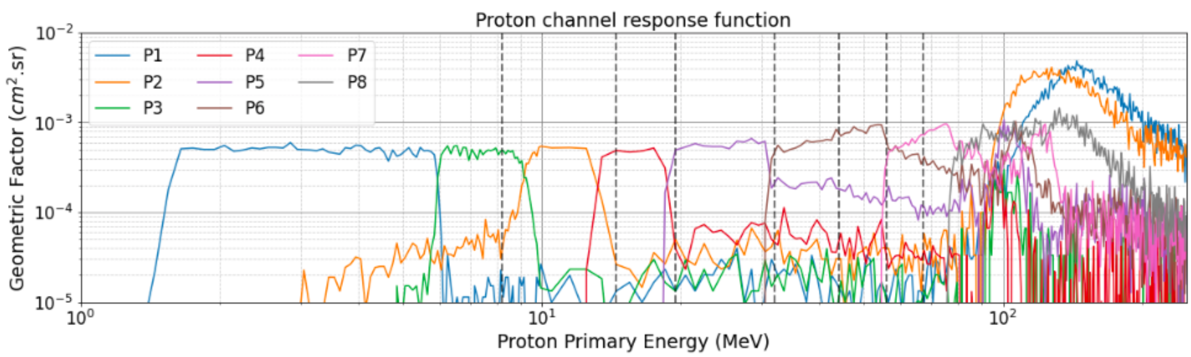

Figure 4.12: Proton channels response functions. Each color corresponds to one proton channel.

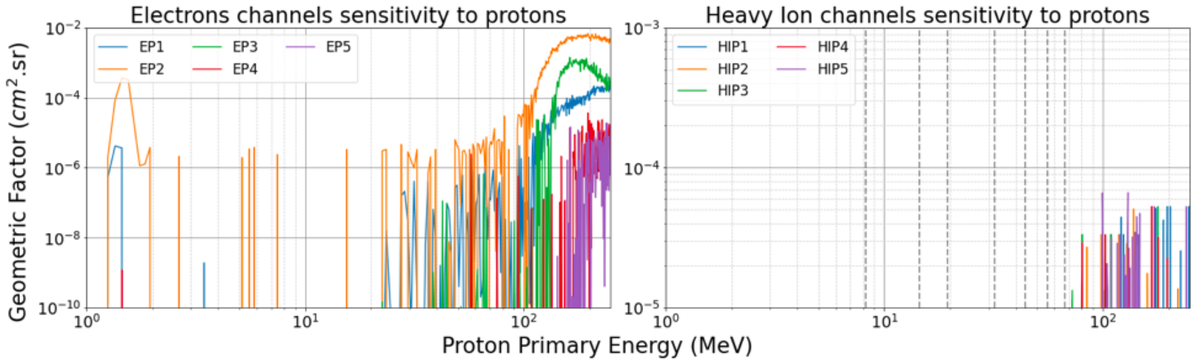

Figure 4.13: Electron channels sensitivity to protons (left). Heavy ion channels sensitivity to protons (right).

Channel	Channel Name	Type	E_{eff}(MeV)	GdE($cm^2 \cdot sr \cdot MeV$)	G_I($cm^2 \cdot sr$)	σ_{min}	δ_G^-		δ_G^+	
6	P1	Dif	2.82	$2.19 \cdot 10^{-3}$	-	0.073	$-1.92 \cdot 10^{-4}$	-9%	$2.69 \cdot 10^{-4}$	12%
7	P2	Dif	12.96	$7.48 \cdot 10^{-3}$	-	0.177	$-1.39 \cdot 10^{-3}$	-17%	$2.72 \cdot 10^{-3}$	36%
8	P3	Dif	7.97	$2.11 \cdot 10^{-3}$	-	0.043	$-1.21 \cdot 10^{-4}$	-6%	$1.44 \cdot 10^{-4}$	7%
9	P4	Dif	17.29	$4.10 \cdot 10^{-3}$	-	0.020	$-8.44 \cdot 10^{-5}$	-2%	$1.42 \cdot 10^{-4}$	3%
10	P5	Dif	28.52	$1.40 \cdot 10^{-2}$	-	0.029	$-4.40 \cdot 10^{-4}$	-3%	$7.75 \cdot 10^{-4}$	6%
11	P6	Int	26.55	-	$4.01 \cdot 10^{-4}$	0.021	$-1.61 \cdot 10^{-5}$	-4%	$8.62 \cdot 10^{-6}$	2%
12	P7	Int	47.18	-	$3.63 \cdot 10^{-4}$	0.033	$-1.81 \cdot 10^{-5}$	-5%	$9.02 \cdot 10^{-6}$	2%
13	P8	Int	71.88	-	$5.58 \cdot 10^{-4}$	0.010	$-1.41 \cdot 10^{-5}$	-3%	$6.15 \cdot 10^{-6}$	1%

Table 4.3: Characteristic energies and geometric factors of proton channels of BERM (P bins). E_{eff} corresponds to the minimum value of the normalized standard deviation σ of the $\{\gamma$,G(E,γ)$\}_E$ distribution. GdE or G_I corresponds to the mean value of $\{\gamma$,G(E,γ)$\}_{E_{Eff}}$, and the errors δ_G^- and δ_G^+ correspond to the fifth and ninety-fifth percentile of the distribution subtracted by the mean value.

Channel	Channel Name	Type	E_{eff}(MeV)	GdE($cm^2 \cdot sr \cdot MeV$)	G_I($cm^2 \cdot sr$)	σ_{min}	δ_G^-		δ_G^+	
6	P1*	Dif	2.47	$1.49 \cdot 10^{-3}$	-	0.021	$-3.39 \cdot 10^{-5}$	-2%	$5.70 \cdot 10^{-5}$	4%
7	P2*	Dif	8.13	$1.77 \cdot 10^{-3}$	-	0.060	$-1.89 \cdot 10^{-4}$	-11%	$1.77 \cdot 10^{-4}$	10%

Table 4.4: Characteristic energies and geometric factors of BERM proton channels P1 and P2, considering only primary energies lower than 90 MeV.

Channel	Channel Name	Type	E_{eff}(MeV)	GdE($cm^2 \cdot sr \cdot MeV$)	G_I($cm^2 \cdot sr$)	σ_{min}	δ_G^-		δ_G^+	
1	EP1	Dif	1.37	$4.17 \cdot 10^{-6}$	-	0.010	$-5.22 \cdot 10^{-9}$	-1%	$5.75 \cdot 10^{-9}$	1%
2	EP2	Dif	1.46	$4.40 \cdot 10^{-5}$	-	0.009	$-3.77 \cdot 10^{-7}$	-0.4%	$5.50 \cdot 10^{-7}$	1%
3	EP3	Dif	184.26	-	$1.07 \cdot 10^{-6}$	0.019	$-1.89 \cdot 10^{-3}$	-3%	$2.71 \cdot 10^{-3}$	4%
4	EP4	Dif	187.96	-	$8.95 \cdot 10^{-7}$	0.047	$-4.68 \cdot 10^{-5}$	-10%	$2.84 \cdot 10^{-5}$	6%
5	EP5	Dif	204.04	-	$3.28 \cdot 10^{-9}$	0.017	$-3.15 \cdot 10^{-7}$	-0.1%	$1.98 \cdot 10^{-6}$	1%

Table 4.5: Characteristic energies and geometric factors of electron channels of BERM measuring protons (EP bins)

Electrons

In the response to electrons, the largest difference was in electron channel E1, which was a value three orders of magnitude higher. Consequently, the fluxes reconstructed with this channel will be higher. The other channels keep similar parameters, with the exception of E5. This channel has a higher effective energy, however the difference from the previous analysis is mainly due to low statistics in the simulation in this energy range. This channels is the one with the higher uncertainty.

Another relevant change is in PE1 (first proton channels contaminated by electrons), which has now a higher effective energy and lower geometric factor.

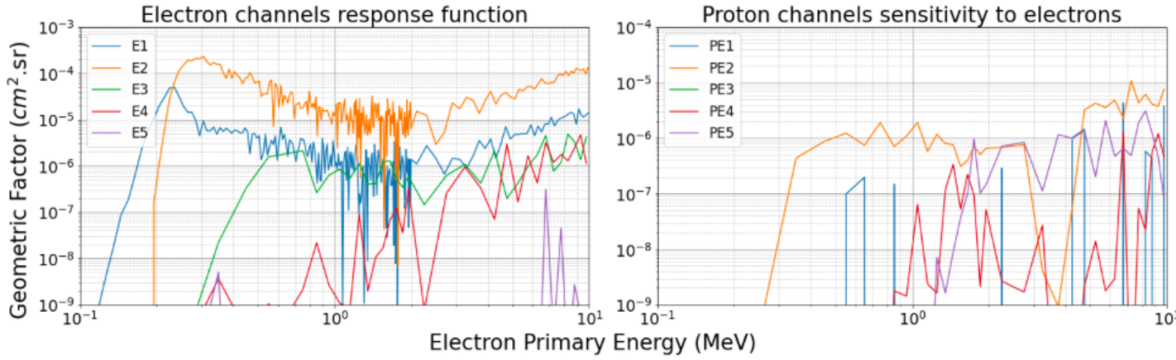

Figure 4.14: Electron channels response function (right). Proton channels sensitivity to electron (right).

Channel	Channel Name	Type	E_{eff}(MeV)	GdE($cm^2 \cdot sr \cdot MeV$)	$G_I(cm^2 \cdot sr)$	σ_{min}	δ_G^-		δ_G^+	
1	E1	Dif	0.25	$4.17 \cdot 10^{-6}$	-	0.026	$-1.13 \cdot 10^{-7}$	-3%	$1.99 \cdot 10^{-7}$	5%
2	E2	Dif	0.34	$4.40 \cdot 10^{-5}$	-	0.030	$-1.48 \cdot 10^{-6}$	-3%	$2.36 \cdot 10^{-6}$	5%
3	E3	Int	0.42	-	$1.07 \cdot 10^{-6}$	0.044	$-1.85 \cdot 10^{-8}$	-2%	$2.23 \cdot 10^{-8}$	2%
4	E4	Int	2.11	-	$8.95 \cdot 10^{-7}$	0.067	$-6.75 \cdot 10^{-8}$	-8%	$9.86 \cdot 10^{-8}$	11%
5	E5	Int	5.23	-	$4.41 \cdot 10^{-8}$	0.145	$-6.07 \cdot 10^{-10}$	-19%	$8.11 \cdot 10^{-10}$	25%

Table 4.6: Characteristic energies and geometric factors of electron channels of BERM (E bins)

Channel	Channel Name	Type	E_{eff}(MeV)	GdE($cm^2 \cdot sr \cdot MeV$)	$G_I(cm^2 \cdot sr)$	σ_{min}	δ_G^-		δ_G^+	
6	PE1	Int	0.75	-	$2.20 \cdot 10^{-7}$	0.100	$-2.43 \cdot 10^{-8}$	-11%	$4.03 \cdot 10^{-8}$	18%
7	PE2	Int	0.37	-	$1.22 \cdot 10^{-6}$	0.051	$-4.87 \cdot 10^{-8}$	-4%	$9.88 \cdot 10^{-8}$	8%
9	PE4	Int	1.18	-	$1.01 \cdot 10^{-7}$	0.038	$-4.50 \cdot 10^{-9}$	-4%	$6.99 \cdot 10^{-9}$	7%
10	PE5	Int	1.97	-	$9.02 \cdot 10^{-7}$	0.010	$-1.00 \cdot 10^{-8}$	-1%	$2.27 \cdot 10^{-8}$	3%
11	PE6	Int	6.18	-	$2.25 \cdot 10^{-7}$	0.013	$-4.75 \cdot 10^{-9}$	-2%	$3.61 \cdot 10^{-9}$	2%
12	PE7	Int	0.16	-	$3.12 \cdot 10^{-11}$	0.083	$-3.85 \cdot 10^{-12}$	-12%	$2.44 \cdot 10^{-12}$	8%
13	PE8	Int	0.85	-	$1.40 \cdot 10^{-9}$	0.034	$-8.59 \cdot 10^{-11}$	-6%	$5.30 \cdot 10^{-11}$	4%

Table 4.7: Characteristic energies and geometric factors of proton channels of BERM measuring electrons (PE bins)

5

BERM Model Validation

Contents

To validate the new BepiColombo Environment Radiation Monitor (BERM) response functions and bow-tie flux reconstruction algorithm, data obtained during the Earth flyby and of two Solar Particle Events (SPEs) observed by both BERM and SIXS-P. Table 5.1 present the effective energies of each channel used in this comparison, were used.

BERM		SIXS-P (Side 0)	
Channel	E_{Eff} (MeV)	Channel	E_{Eff} (MeV)
E1 E2	0.25 0.34	E4	0.28
P1	2.82	P4	2.26
P2	12.96	P6	8.02
P3	7.97	P7	14.3

Table 5.1: BERM and SIXS-P channels used in the analysis of the SEP event.

5.1 Earth Flyby

Figure 5.1 shows the comparison between BERM's and SIXS-P's data. All channels are in better closer agreement when compared to previous results (see figure 3.15). There are two main differences in this analysis: the pitch angle and the flux reconstruction.
The pitch angle, is defined as the angle between the magnetic field lines and the normal to the entrance plane of the detector. This means that under anisotropic flux BERM does not have the same response as SIXS-P since they do not point in the same direction (see figure 5.3 left). To convert the fluxes to the same pitch angle, the relation between fluxes and pitch angle was fitted with Legendre Polynomials, represented in equation 5.1. To fit the relation between this to quantities in the Earth radiation belts, it is only necessary to use the first six Legendre coefficients. Imposing symmetry around $\alpha = 90°$, all odd coefficients must be zero, leaving only n=2,4,6. In figure 5.2, the fluxes of each channel in Figure 5.1, converted to the pitch angle of SIXS-P S0, are presented. As it can be seen, the fluxes obtained with BERM E1 and SIXS-P E4 during the Earth flyby are in close agreement, validating the model built in this thesis. It is also important to notice that as a result of this analysis, proton channels that were already in agreement between BERM and SIXS-P, continue to do so.

$$F(\alpha) = |C_0| \sum_{n=1}^{6} c_n P_n(\alpha) \tag{5.1}$$

Having corrected the data with the pitch angle, there are still some differences in the measured fluxes. In the inner belt, dominated by protons, proton contamination can be seen in BERM channel E2. This channel has high sensitivity to protons as shown in figure 4.13. Geometric factor of E2 and EP2 are in the same order of magnitude to low energies. The same does not verify for E1 and EP1. For the same energy range, E1 is more than four order of magnitude higher than EP1. As a consequence, E2 is much more contaminated by protons than E1.

The reconstructed particle fluxes were also compared with the AE8/9 and AP8/9 models. In figure 5.4, the spectra obtained with BERM, SIXS-P and models AE8/9 and AP8/9 are presented. Figure 5.4 (left) shows the inner belt is dominated by protons. This figure presents BERM channels P1-P3, EP1-EP2 and SIXS-P proton channels of SIXS-P side 0-3. In both cases the results are close to the models, meaning that both the proton channels response functions and electron channels contamination are correctly modeled. Figures 5.4 (right) shows the outer belt, dominated by electrons, where BERM channels E1-E2 and SIXS-P side 0 electron channels are presented. Side 0 was the only SIXS-P side turned on at the time off the flying. In both cases, the spectra agrees with the models predictions, validating BERM data.

The relation between BERM and SIXS-P data, and BERM data and A8/A9 models during the Earth flyby is the major result obtained in this work. It validates the new BERM model, which better describes the instrument's response to electrons, more specifically, to low energy electrons assigned to E1, a channel that was unable to produce any relevant scientific result. The significance of this result is extended due to the fact that this channel has the lowest effective energy. The detection of low energetic electrons is very important during BepiColombo mission, therefor it is of major interest to have a reliable model of the first electron channels.

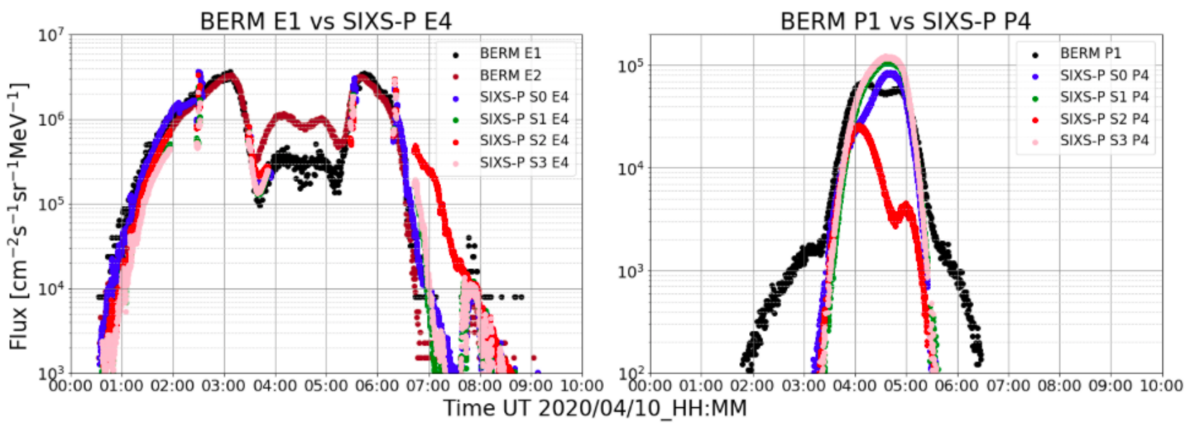

Figure 5.1: Left: Data comparison between BERM channel E1 and SIXS-P channel E4 during the Earth fly-by. Right: Data comparison between BERM channel P1 and SIXS-P channel P4 during the Earth fly-by.

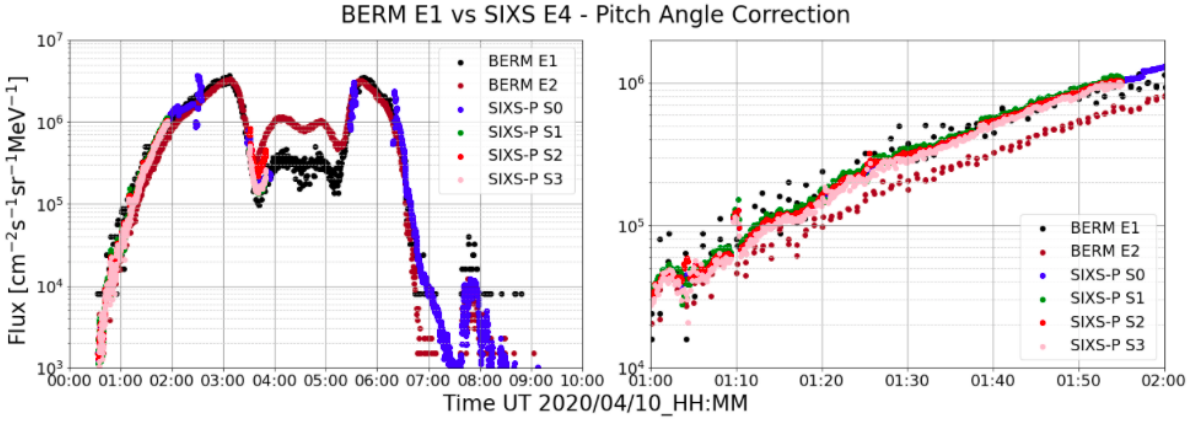

Figure 5.2: Left: Data comparison between BERM channel E1 and SIXS-P channel E4 during the Earth fly-by, with all channels flux converted to SIXS-P S0 pitch angle. Right: Detailed view of the outer belt.

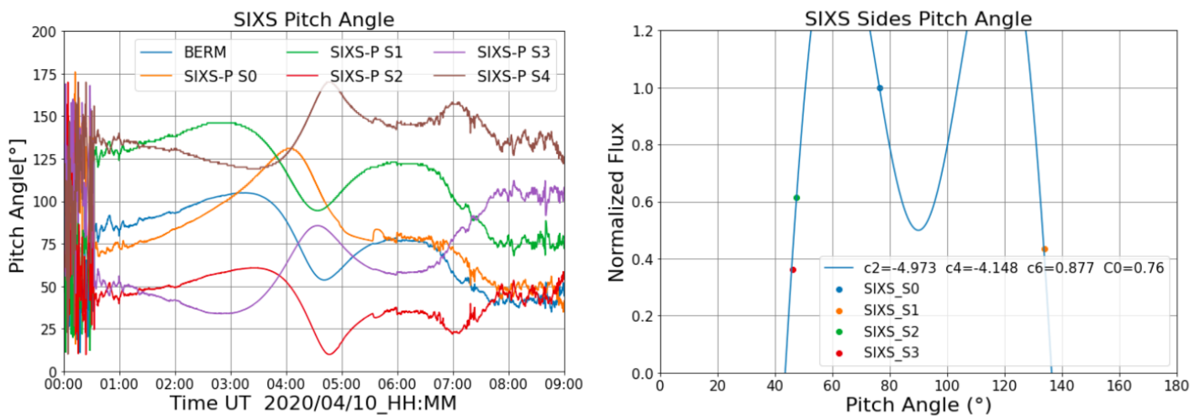

Figure 5.3: Left: BERM and SIXS-P pitch angle during the Earth fly-by. Right: example of SIXS-P pitch angle fitted with Legendre polynomials.

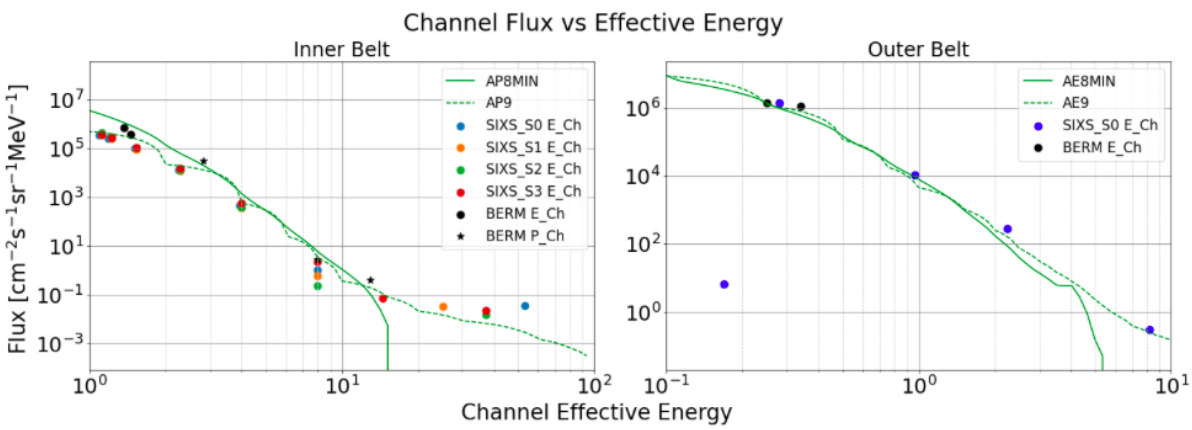

Figure 5.4: Earth radiation belts spectra obtained with BERM, SIXS-P and models AP8,AP9, AE8 and AE9. Left: Inner belt, Right: Outer Belt

5.2 Solar Energetic Particle Event

During September of 2022 there was a Solar Energetic Particle event detected by BERM and SIXS-P. Figure 5.5 presents BERM channels E1 and E2 and SIXS-P channels E4. Figure 5.6 presents BERM channels P1-P3 and SIXS-P channels P4, P6 and P7. Compared to the Earth flyby, this event had a lower flux, affecting the analysis of BERM, especially in the electron channels. Due to the characteristics of the detectors, BERM has lower geometric factors than SIXS-P, resulting in more detailed features observed by SIXS-P. Nevertheless, during the entire event there are some features seen simultaneously and in good agreement between both instruments. To obtain these figures BERM fluxes were integrated over one hour and SIXS fluxes were integrated within 7.5 minutes. The time intervals of integration were chosen in order to minimise statistical fluctuation without losing too much detail.

In the entire event, figure 5.5 a), it can be seen that the three channels with similar effective energy show a similar flux, both in terms of time evolution of the event and of particle flux at each moment. Figure 5.5 also presents closeups of three time periods; first an increase in the particle flux with the duration of approximately 1 days (b), followed by a slower decrease (c) with the duration of approximately 10 days. The third moment presents a faster increase and decrease of the particle flux with a total duration of approximately 3 days (d).

In the first time period, figure 5.5 b), all three channels follow the same spectrum. BERM channel E1, due to the lower statistics does not present every feature with detail but follows the main trend, especially for higher fluxes. BERM channel E2, shows more details. As an example, between 0h and 6h of 7th of September, there was a short increase in the particle flux detected with both SIXS-P E4 and BERM E2.

In the second time period shown in figure 5.5 c), the agreement between both detectors is even more evident, with every small feature being seen simultaneously by the three channels. A good example are the oscillations in the flux registered at 9th of September and between 13th and 14th of September.

The third time period, figure 5.5 d), exhibits lower fluxes which means higher uncertainties, especially for BERM. Even so, one characteristic that can be notice is that this part of the event has similar fluxes of protons and electrons, increasing the contamination of BERM E2. The time evolution of the flux of BERM E2 is also similar with proton flux presented in figure 5.6. At 25th of September there is a small rise in electron and proton flux, followed by a prominent decrease in electron flux but not in proton flux. For protons, after this peak the fluxes either decrease slowly or remain constant. This behaviour is also seen in BERM E2, meaning its observations are contaminated by protons.

Proton channels, also display a good agreement between each other, shown in figures, 5.6 b) to 5.6 d), where BERM and SIXS-P always present the same features.

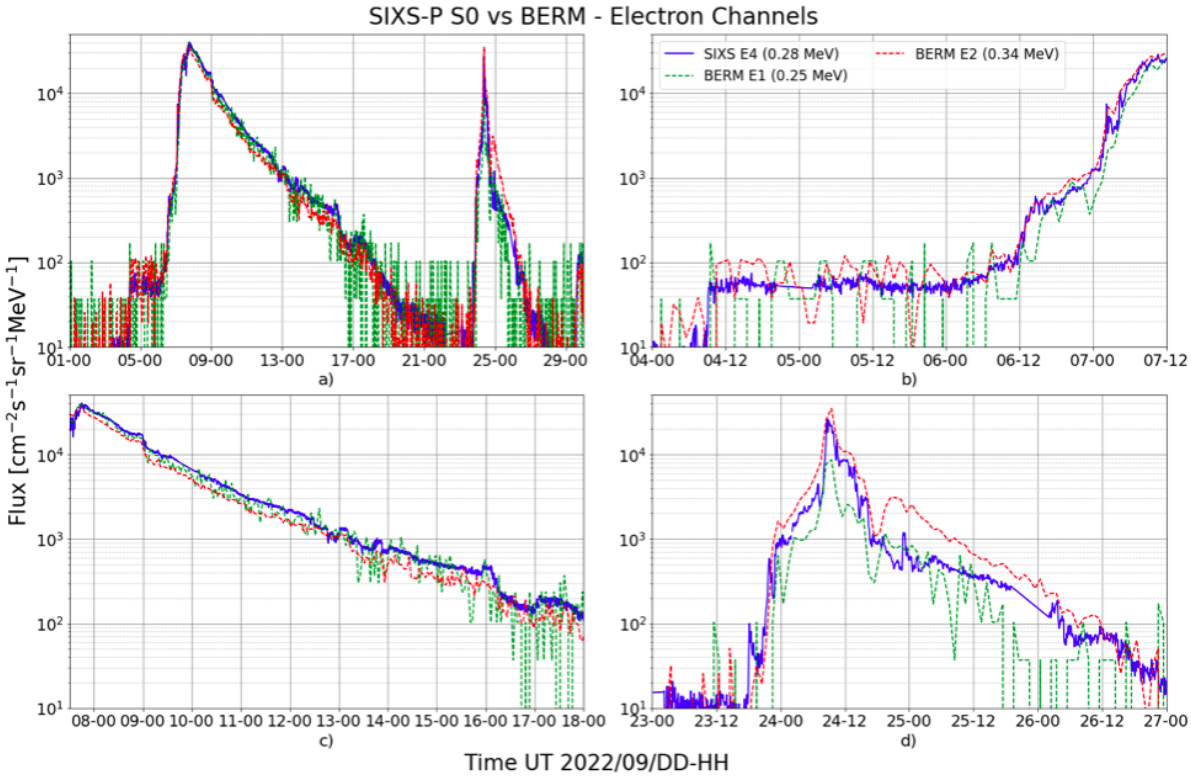

Figure 5.5: Comparison between SIXS-P and BERM electron channels during Solar energetic particle event. a) Global view of the entire event. b) Close view of the increasing of the flux between 2022-09-04 00:00 to 2022-09-07 12:00. c) Close view of the decreasing of the flux between 2022-09-07 12:00 to 2022-09-18 00:00. d) Close view of the second part of the event between 2022-09-23 00:00 to 2022-09-27 00:00.

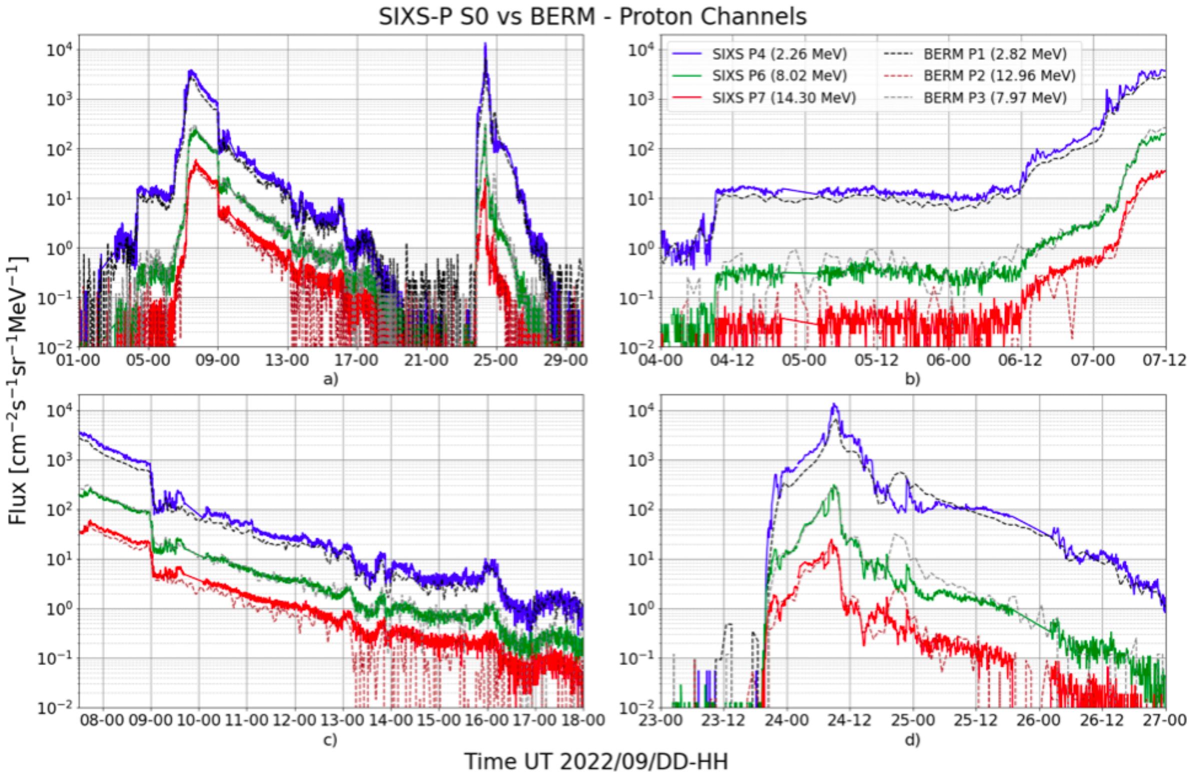

Figure 5.6: Comparison between SIXS-P and BERM proton channels during Solar energetic particle event. a) Global view of the entire event. b) Close view of the increasing of the flux between 2022-09-04 00:00 to 2022-09-07 12:00. c) Close view of the decreasing of the flux between 2022-09-07 12:00 to 2022-09-18 00:00. d) Close view of the second part of the event between 2022-09-23 00:00 to 2022-09-27 00:00.

6

Conclusion

Contents

In this work, the response functions of the BepiColombo Environment Radiation Monitor (BERM) were reassessed, based on new experimental data and modeling. The starting point of this work was the analysis of BERM Earth flyby data. Low energy electron observations were not in agreement with SIXS-P and the the AE8 and AP8 Van Allen belt models. The first part of this thesis was centred on testing the BERM Engineering Qualification Model (EQM) model with 90-Sr and 137-Cs radioactive sources to investigate the underlying cause of BERM response shortcomings. With the new set of experimental data, three parameters were analysed: the detector trigger threshold, noise and cross-talk between detectors. Changing the trigger threshold value can produce a significant difference in BERM response functions. However, the analysis of this parameter showed only a small difference from the value previously obtained during BERM calibration.

The electrical noise in the detectors can also affect the behaviour of BERM. A deeper analysis of the noise in all detectors was taken in consideration in this work. The result presents a closer agreement between BERM´s data and simulation, mainly in the contamination of proton channel ♯8 with electron. However, electron channels do not change significantly their result.

Looking to the experimental data taken with EQM model in 2D plots of detector i vs detector i+1, a feature not seen in the simulation, was found. This was compatible with cross-talk in the detectors. In this case detectors are sharing between 20-30 % of their energy to the adjacent detector. The cross-talk exhibits an asymmetric behaviour. Cross-talk between detectors is common to occur, however the intensity is higher than expected and the fact that it occurs in one direction only is still not explained.

The cross-talk models developed in this thesis were added to the response function of BERM. Electron fluxes of the Earth flyby were reconstructed using a bow-tie method applied to the new response functions. The results were in good agreement with SIXS-P data. This is especially noticeable in BERM's first electron channel which were previously off by a factor of 1000. Proton fluxes were still in good agreement further validating the methods developed in this thesis. The new model was also validated with data from a SEP event that impacted BepiColombo in September 2022. This was a good event to test the analysis present in this work due to its complexity, exhibiting two separate peaks. The first one with a higher prominence of electrons and characterised by a fast rise followed by a slow decrease in the particle flux. In the second peak, the proton flux was higher compared to the first one, and the time evolution was also different. Particle fluxes calculated with both instruments were also in good agreement in this peak.

These results show that the model to the cross-talk developed in this thesis is fundamental to describe BERM's response to electrons. The characteristics of these phenomena still raise some questions, mainly related with to the cross-talk intensity and its asymmetry between consecutive channels. However the results are very promising, and the model developed in this work is very successful in reconstructing electron and proton fluxes measured by BERM during the BepiColombo mission.

6.1 Future Work

The work performed in this thesis left three main points to be analysed in the future.

The first point is the need for a deeper analysis of the electronics of BERM. This is important to try to comprehend what is behind the cross-talk found in this work. While this feature was characterised, data analysis would benefit from a deeper understating of this behaviour, since any deviation in the electronics of the detector can have a great impact on data.

The second aspect is the need to use other methods to reconstruct particle fluxes from BERM measurements. The bow-tie method can be used as a first approach, however it has some drawbacks. The bow-tie performs a weighted average of the energy range and geometric factor of each channel, and assumes an energy spectrum described by a power law. In a future analysis, the combined channels response function should be taken in consideration in BERM particle flux reconstruction. Methods like neural networks or Single Value Decomposition take this in consideration, resulting in more realistic particle flux reconstruction [32, 33].

The third analysis left for a future work is the characterisation of BERM channels with heavy ions. So far, in this work and in [10], only electrons and protons have been analysed.

Bibliography

[1] Pinto, M. *et al.* The bepicolombo environment radiation monitor, berm. *Space Science Reviews* **218**, 54 (2022). URL https://doi.org/10.1007/s11214-022-00922-2.

[2] Mangano, V. *et al.* Bepicolombo science investigations during cruise and flybys at the earth, venus and mercury. *Space Science Reviews* **217**, 23 (2021). URL https://doi.org/10.1007/s11214-021-00797-9.

[3] Milillo, A. *et al.* Investigating mercury's environment with the two-spacecraft bepicolombo mission. *Space Science Reviews* **216**, 93 (2020). URL https://doi.org/10.1007/s11214-020-00712-8.

[4] Giberson, W. & Cunningham, N. Mariner 10 mission to venus and mercury. *Acta Astronautica* **2**, 715–743 (1975). URL https://www.sciencedirect.com/science/article/pii/0094576575900120.

[5] McNutt, R. L., Solomon, S. C., Gold, R. E. & Leary, J. C. The messenger mission to mercury: Development history and early mission status. *Advances in Space Research* **38**, 564–571 (2006). URL https://www.sciencedirect.com/science/article/pii/S0273117705006198. Mercury, Mars and Saturn.

[6] Benkhoff, J. *et al.* Bepicolombo - mission overview and science goals. *Space Science Reviews* **217**, 90 (2021). URL https://doi.org/10.1007/s11214-021-00861-4.

[7] Huovelin, J. *et al.* Solar intensity x-ray and particle spectrometer sixs: Instrument design and first results. *Space Science Reviews* **216**, 94 (2020). URL https://doi.org/10.1007/s11214-020-00717-3.

[8] Mitrofanov, I. G. *et al.* The mercury gamma-ray and neutron spectrometer (mgns) onboard the mercury planetary orbiter of the bepicolombo mission: Design updates and first measurements in space. *Space Science Reviews* **217**, 67 (2021). URL https://doi.org/10.1007/s11214-021-00842-7.

[9] Murakami, G. *et al.* Mio—first comprehensive exploration of mercury's space environment: Mission overview. *Space Science Reviews* **216**, 113 (2020). URL https://doi.org/10.1007/s11214-020-00733-3.

[10] Cardoso, C. *Flight data analysis of the BERM radiation monitor aboard the BepiColombo mission to Mercury*. Master's thesis, Instituto Superior Técnico (2020).

[11] Chitta, L. P. *et al.* Picoflare jets power the solar wind emerging from a coronal hole on the sun. *Science* **381**, 867–872 (2023). URL https://www.science.org/doi/abs/10.1126/science.ade5801. https://www.science.org/doi/pdf/10.1126/science.ade5801.

[12] Turner, R. Solar particle events from a risk management perspective. *IEEE Trans Plasma Sci IEEE Nucl Plasma Sci Soc* **28**, 2103–2113 (2000).

[13] Reames, D. V. Particle acceleration at the sun and in the heliosphere. *Space Science Reviews* **90**, 413–491 (1999).

[14] Reames, D. V. Magnetic topology of impulsive and gradual solar energetic particle events. *The Astrophysical Journal* **571**, L63 (2002). URL https://dx.doi.org/10.1086/341149.

[15] Van Allen, J. A., Ludwig, G. H., Ray, E. C. & McIlwain, C. E. Observation of high intensity radiation by satellites 1958 alpha and gamma. *Jet Propulsion* **28** (1958). URL https://www.osti.gov/biblio/4300875.

[16] Barth, J., Dyer, C. & Stassinopoulos, E. Space, atmospheric, and terrestrial radiation environments. *IEEE Transactions on Nuclear Science* **50**, 466–482 (2003).

[17] Vainio, R. *et al.* Dynamics of the earth's particle radiation environment. *Space Science Reviews* **147**, 187–231 (2009).

[18] ESA. Earth's plasmasphere and the van allen belts (1/09/2019). URL https://sci.esa.int/web/cluster/-/52831-earth-plasmasphere-and-the-van-allen-belts. Accessed 19-October-2023.

[19] ESA. Illustration showing van allen radiation belts (2016). URL https://www.esa.int/ESA_Multimedia/Images/2016/06/Illustration_showing_Van_Allen_radiation_belts. Accessed 12-October-2023.

[20] Slavin, J. Mercury's magnetosphere. *Advances in Space Research* **33**, 1859–1874 (2004).

[21] Ho, G. C. *et al.* Messenger observations of transient bursts of energetic electrons in mercury's magnetosphere. *Science* **333**, 1865–1868 (2011). URL https://www.science.org/doi/abs/10.1126/science.1211141. https://www.science.org/doi/pdf/10.1126/science.1211141.

[22] Lawrence, D. J. *et al.* Comprehensive survey of energetic electron events in mercury's magnetosphere with data from the messenger gamma-ray and neutron spectrometer. *Journal of Geophysical Research: Space Physics* **120**, 2851–2876 (2015). URL https://agupubs.onlinelibrary.wiley.com/doi/abs/10.1002/2014JA020792. https://agupubs.onlinelibrary.wiley.com/doi/pdf/10.1002/2014JA020792.

[23] Baker, D. N. *et al.* Intense energetic electron flux enhancements in mercury's magnetosphere: An integrated view with high-resolution observations from messenger. *Journal of Geophysical Research: Space Physics* **121**, 2171–2184 (2016). URL https://agupubs.onlinelibrary.wiley.com/doi/abs/10.1002/2015JA021778. https://agupubs.onlinelibrary.wiley.com/doi/pdf/10.1002/2015JA021778.

[24] Berger, M.J., Coursey, J.S., Zucker, M.A., and Chang, J. ESTAR, PSTAR, and ASTAR: Computer Programs for Calculating Stopping-Power and Range Tables for Electrons, Protons, and Helium Ions (2005). URL http://physics.nist.gov/Star. Accessed 16-January-2023.

[25] Dixon, A. 23 - review of solid state physics. In DIXON, A. & LESLIE, J. (eds.) *Solar Energy Conversion*, 773–784 (Pergamon, 1979). URL https://www.sciencedirect.com/science/article/pii/B9780080247441500280.

[26] Sadrozinski, H.-W. Applications of silicon detectors. *IEEE Transactions on Nuclear Science* **48**, 933–940 (2001).

[27] Rancoita, P. G. Silicon detectors and elementary particle physics. *Journal of Physics G: Nuclear Physics* **10**, 299 (1984). URL https://dx.doi.org/10.1088/0305-4616/10/3/007.

[28] CERN. *GEANT4 A simulation toolkit, Physics manual release 11.1*. CERN (2023). URL https://geant4-userdoc.web.cern.ch/UsersGuides/PhysicsReferenceManual/fo/PhysicsReferenceManual.pdf.

[29] Pinto, M. & Gonçalves, P. Guimesh: A tool to import step geometries into geant4 via gdml. *Computer Physics Communications* **239**, 150–156 (2019). URL https://www.sciencedirect.com/science/article/pii/S0010465519300438.

[30] Ginet, G. P. *et al.* Ae9, ap9 and spm: New models for specifying the trapped energetic particle and space plasma environment. *Space Science Reviews* **179**, 579–615 (2013). URL https://doi.org/10.1007/s11214-013-9964-y.

[31] Lauenstein, J.-M. & Barth, J. Radiation belt modeling for spacecraft design: model comparisons for common orbits. In *IEEE Radiation Effects Data Workshop, 2005.*, 102–109 (2005).

[32] Arruda, L. *et al.* Electrons in geo measured with the esa multifunctional spectrometer during the january 2014 sep. *IEEE Transactions on Nuclear Science* **65**, 1540–1545 (2018).

[33] Sandberg, I. *et al.* Unfolding and validation of srem fluxes. In *2011 12th European Conference on Radiation and Its Effects on Components and Systems*, 599–606 (2011).

A

90-Sr Source - All BERM Detectors

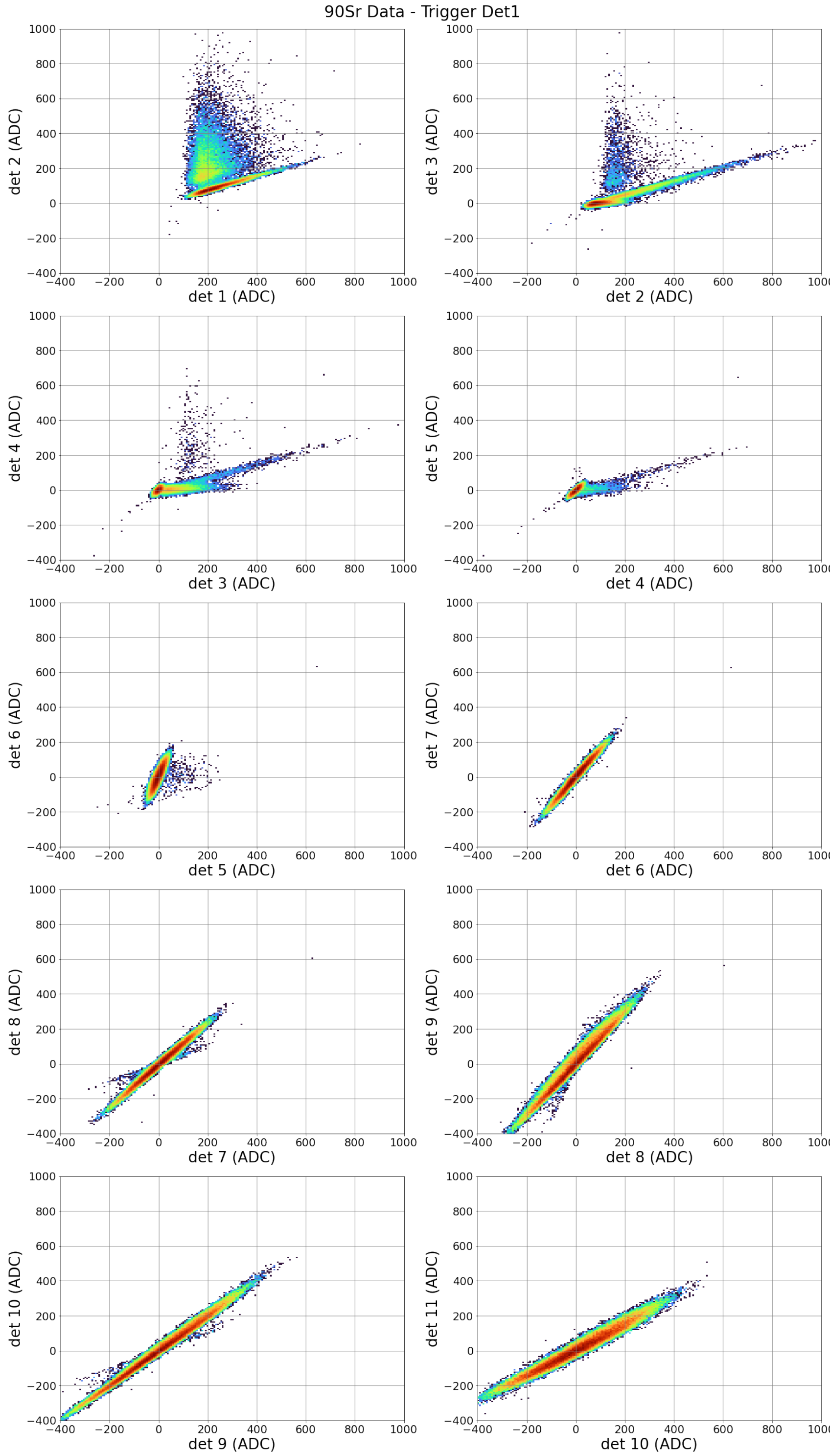

Figure A.1: Relation between signal of consecutive BERM detectors with 90-Sr source. In last plost is possible to see the correlation between noise in the detectors.

B

All BERM Channels - Earth Flyby

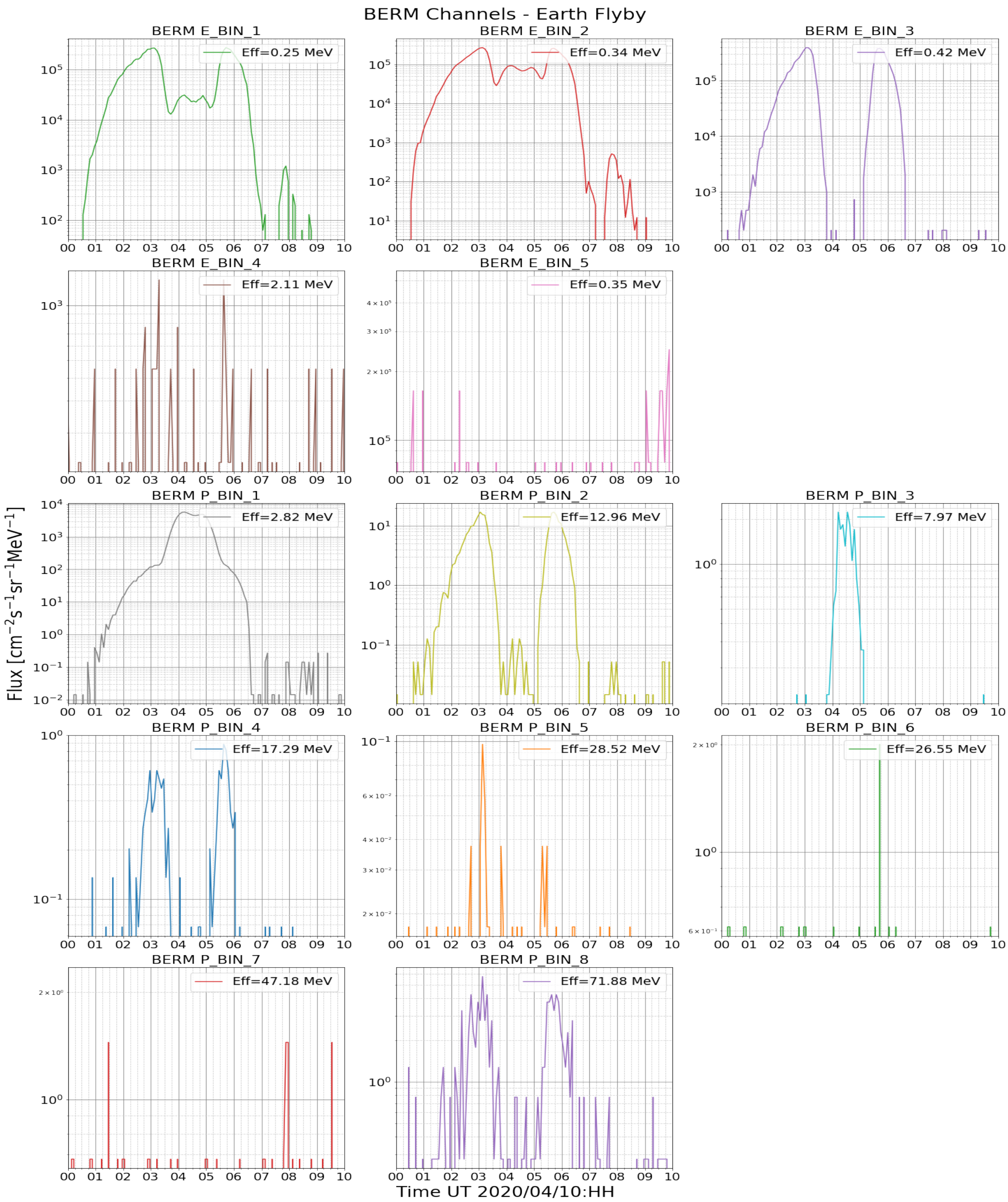

Figure B.1: All BERM channels during the Earth flyby occurred in April 2020.

C

All BERM Channels - SEP Event

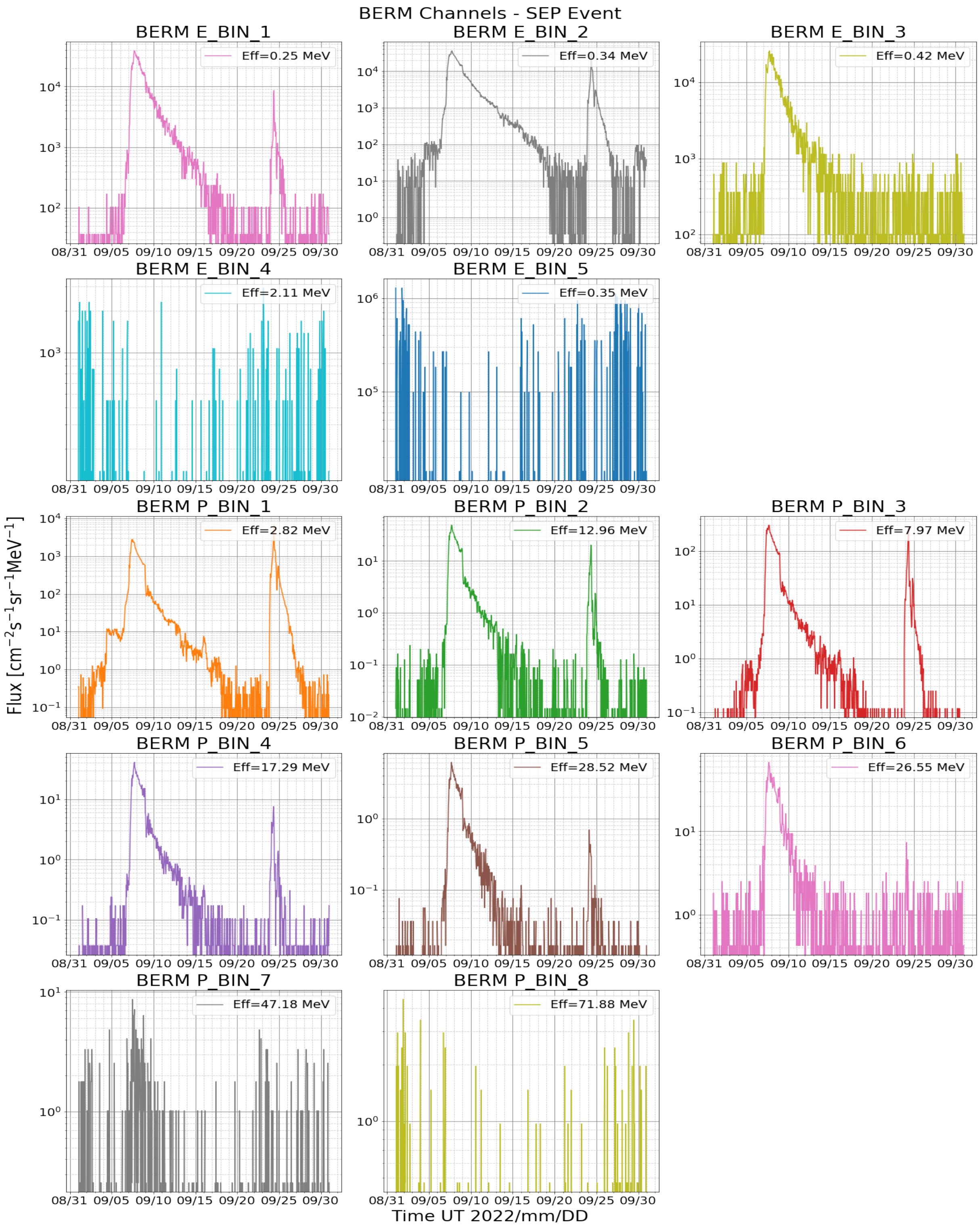

Figure C.1: All BERM channels during the SEP event occurred in September 2022.